

~~SECRET~~
ATSS-16

ASE-1003B

N66-14972

FACILITY FORM 502

(ACCESSION NUMBER) 79	(THRU) 3
(PAGES) 30	(CODE) 30
(NASA CR OR TMX OR AD NUMBER)	(CATEGORY)

**SOME OBSERVATIONAL ASPECTS
OF X-RAY ASTRONOMY**

Based on Lectures delivered by
Riccardo Giacconi

at the
"High Energy Astrophysics"
Course
of the
International School of Physics
Enrico Fermi

Varonna, Italy

July 1965

SOME OBSERVATIONAL ASPECTS OF X-RAY ASTRONOMY

R. Giacconi, H. Gu sky and J. R. Waters
American Science and Engineering, Inc., Cambridge, Massachusetts

B. Rossi, G. Clark, G. Garinire, M. Oda and M. Wada
Massachusetts Institute of Technology, Cambridge, Massachusetts

1.0 INTRODUCTION

The first totally unexpected result of space astronomy was the discovery of strong X-ray sources outside the solar system.

Because of atmospheric absorption, X-rays, of course, cannot be observed with land-based instruments. The altitude requirements for X-ray astronomy become clear from an examination of Fig. 1, showing the altitude where electromagnetic waves of different wavelengths arrive with different degrees of attenuation ($1/2$, $1/10$, $1/100$). One sees that X-rays with wavelength λ greater than about one A (quantum energy E smaller than 12 keV) can be observed only at altitudes greater than 50 km, which can be reached only by rockets or space vehicles. X-rays with quantum energies E greater than about 15 keV, on the other hand, penetrate to altitudes of the order of 30 km, which are within the range of balloon flights.

Even beyond the atmosphere, X-ray astronomy is limited by the absorption in interstellar space. This is shown in Fig. 2; the curves represent the density of interstellar matter (in atoms per cm^3) times the distance (in light years) corresponding to various degrees of attenuation, plotted against wavelength. Since the average density of interstellar

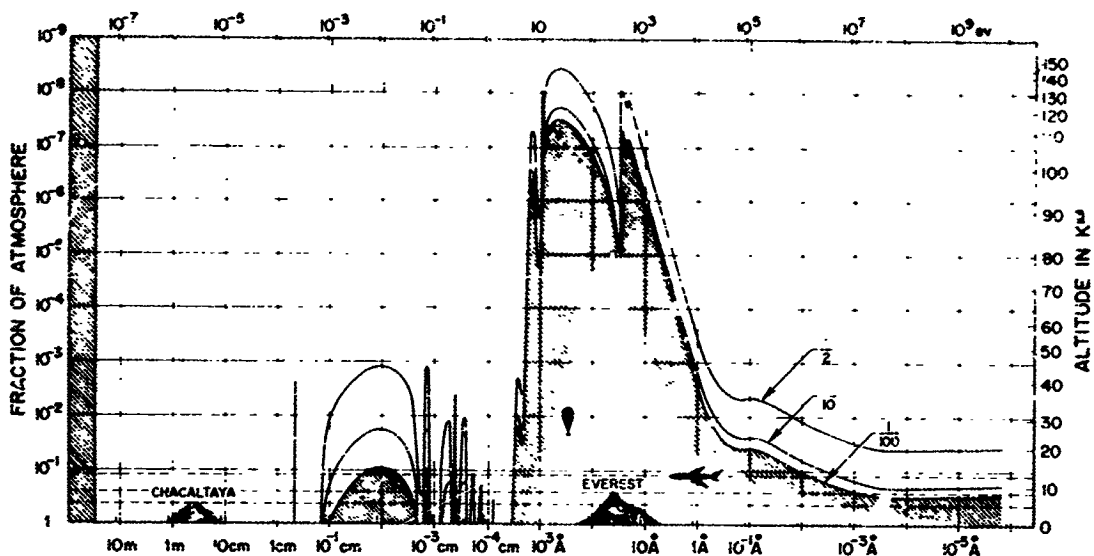


Fig. 1 Attenuation of electromagnetic radiation in the atmosphere. Solid curves indicate altitude (and corresponding pressure expressed as a fraction of one atmosphere) at which a given attenuation occurs for radiation of a given wavelength.

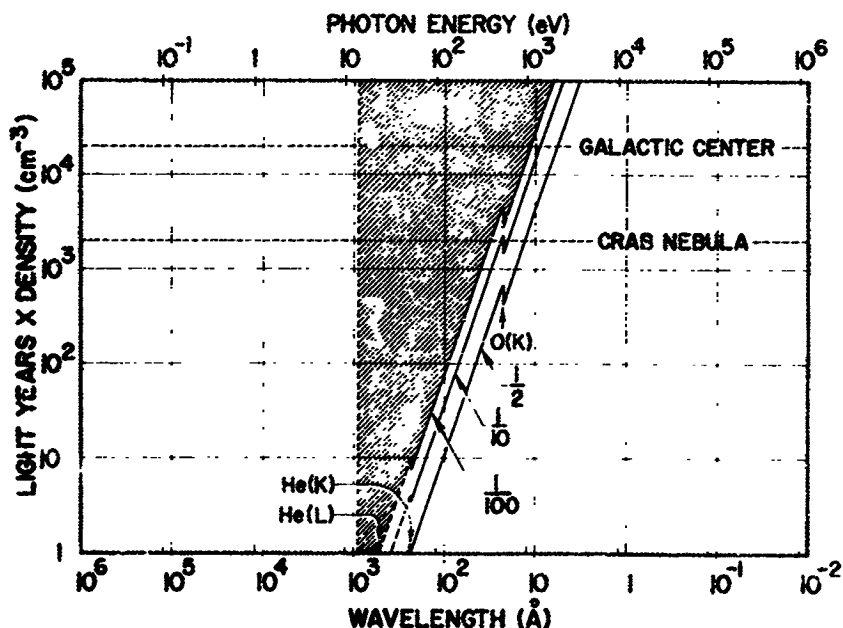


Fig. 2 Attenuation of electromagnetic radiation in interstellar space. The ordinate represents the integrated particle density in terms of light years times the number of particles per cc. The solid curves give the integrated density at which a given attenuation occurs for radiation of a given wavelength. O(K), He(K) and He(L) indicate the K absorption edges of O and He, and the L absorption edge of He. The ordinates corresponding to the Crab Nebula and the galactic center are calculated using the known distance to these objects and an assumed particle density of 0.3 atoms per cc. and one atom per cc. respectively.

matter is of the order of $0.3 \text{ atoms per cm}^3$, we see that, for wavelengths less than about 6\AA , the whole Galaxy is essentially transparent; while X-rays with wavelengths greater than about 100\AA can reach the earth only from sources closer than 100 light years.

Extrasolar X-rays were first detected by means of a rocket launched in June 1962 by Giacconi, Gursky, Paolini of AS&E and Rossi of MIT.⁽¹⁾ The detectors were Geiger counters without a collimator and, therefore, with a wide field of view. The results revealed the existence of a strong source in the constellation Scorpius not far from the galactic center, of a possible secondary source in the constellation of Cygnus and of a diffuse X-ray background, apparently also of celestial origin. Two additional rocket experiments by the same group (October 1962 and June 1963),⁽²⁾ with similar instrumentation, confirmed these results and gave a slight indication of another source in the general direction of the Crab Nebula. In the meantime, (April 1963), a collimated counter, flown by a group at the Naval Research Laboratory under H. Friedman, again detected the Scorpio source.⁽³⁾ The improved resolution made it possible to place an upper limit of 5° to its angular diameter and to determine its location with an accuracy of about 2° . Since the galactic center was below the horizon at the time of this flight, the X-ray source was certainly not coincident with the galactic center. The same flight provided clear evidence for another weaker source in Taurus, within about 2° of the Crab Nebula, and also confirmed the existence of the diffuse background.

In July 1964, the NRL group, using a pointing rocket, succeeded in observing the occultation of the Crab Nebula by the Moon.⁽⁴⁾ This remarkable experiment showed that the X-ray source in Taurus was indeed

coincident with the Crab Nebula and had a full width of about 1 arc minute.

In addition to this flight, five other rocket flights were carried out in 1964, two by the NRL group, two by the AS&E-MIT group, and one by a group at Lockheed headed by Fisher. These flights reconfirmed the source in Scorpius. They also detected a complex of sources in the galactic plane, clustered within about 20° of the galactic center, and some additional sources in the constellations of Cygnus and Serpens.

The year 1964 saw also the first successful attempt to observe X-rays from celestial objects by means of balloon-borne instruments.⁽⁵⁾

Figure 3 shows the region of the sky that has been explored thus far, and the approximate locations of the X-ray sources that have been detected.

2.0 INSTRUMENTATION

2.1 X-ray Detectors

A necessary requirement of the detectors for X-ray astronomy is high efficiency and large effective area because the flux of X-rays from celestial sources, although stronger than had been anticipated, is quite small.

The detectors used so far belong to three different categories.

2.1.1 Gas Counters (Geiger counters and proportional counters).

These instruments may be made in a variety of sizes and shapes. Figure 4 shows a typical design. Their operation as X-ray detectors is based primarily on the production of secondary electrons by the photoelectric

X-RAY SOURCE MAP IN GALACTIC COORDINATES (Equal Area Projection)

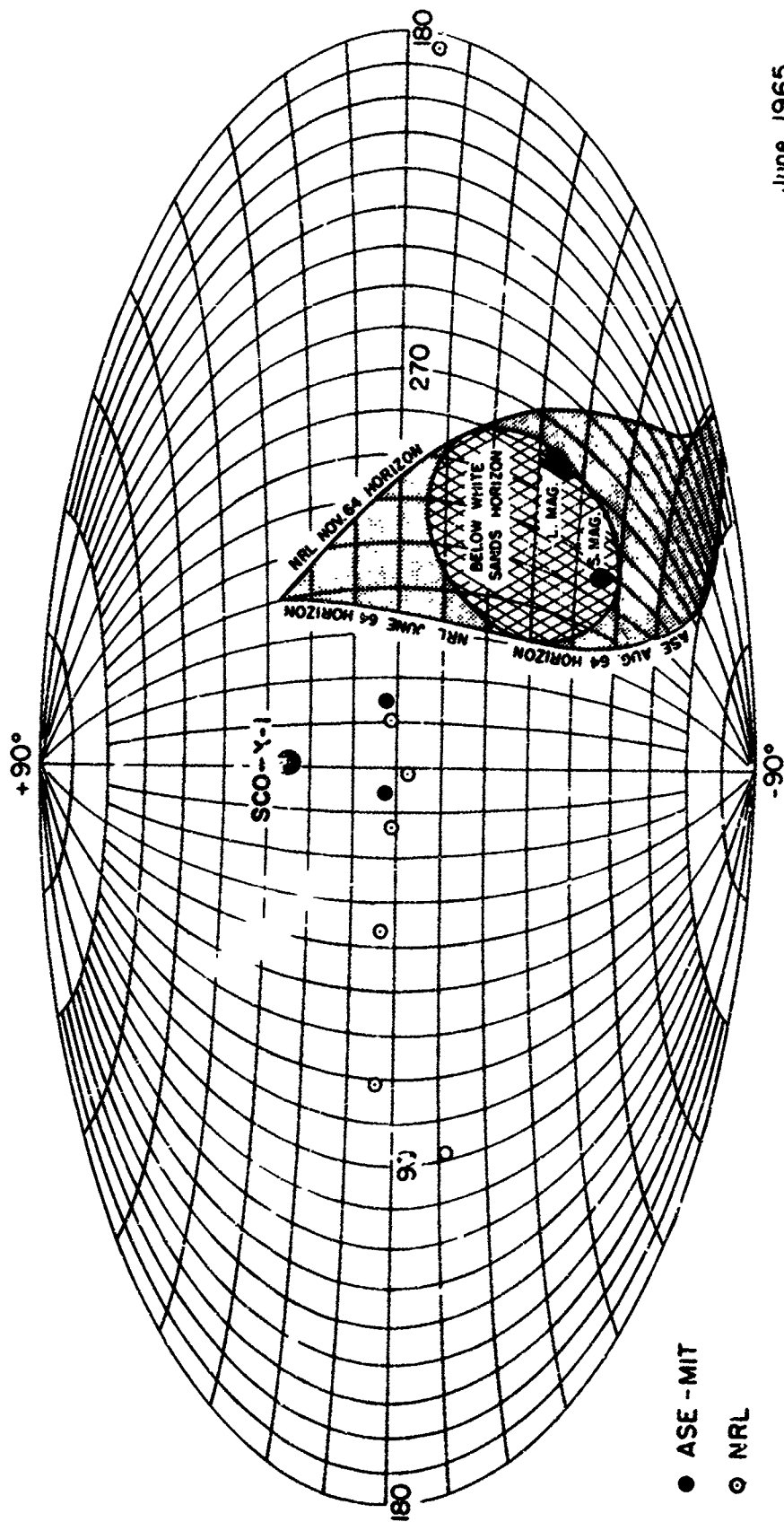


Fig. 3 X-ray source locations in the galactic coordinate system (a II, bII). Cross-hatched region is not observable at the White Sands Missile Range. Shaded region is accessible but was not scanned in the rocket flights performed so far. This region includes the large Magellanic Cloud (L. Mag.) and the Small Magellanic Cloud (S. Mag.). The minimum detectable source intensity in the surveyed region is about 0.05 of the intensity of ScoX-1.

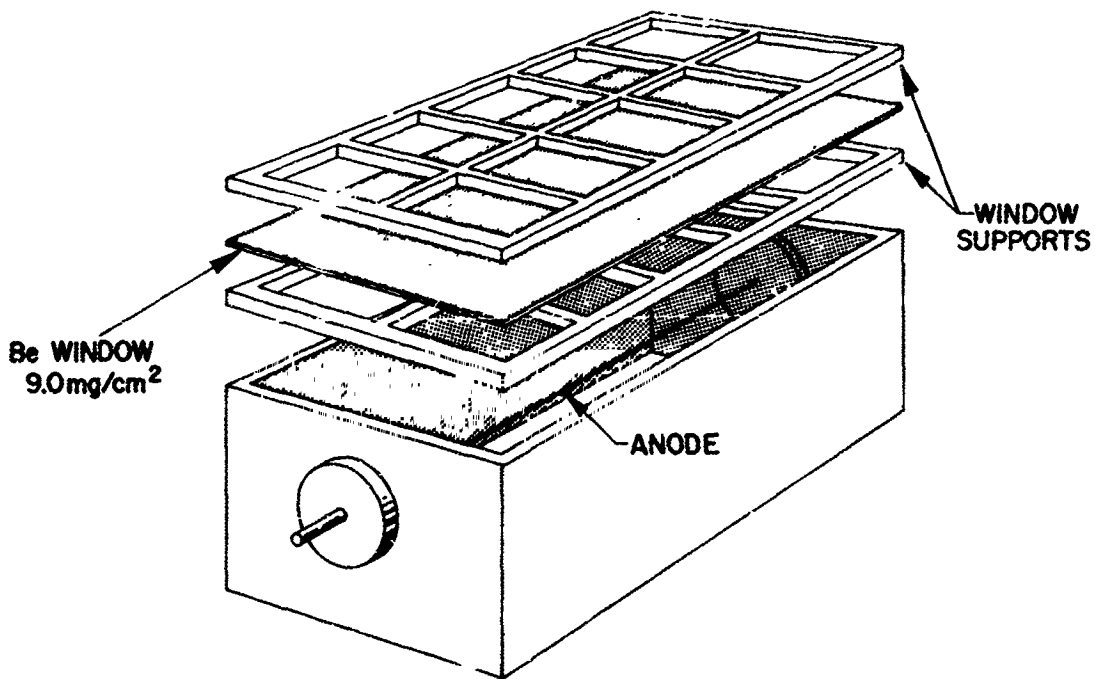


Fig. 4 Schematic drawing of a thin-window gas counter used for the detection of soft X-rays.

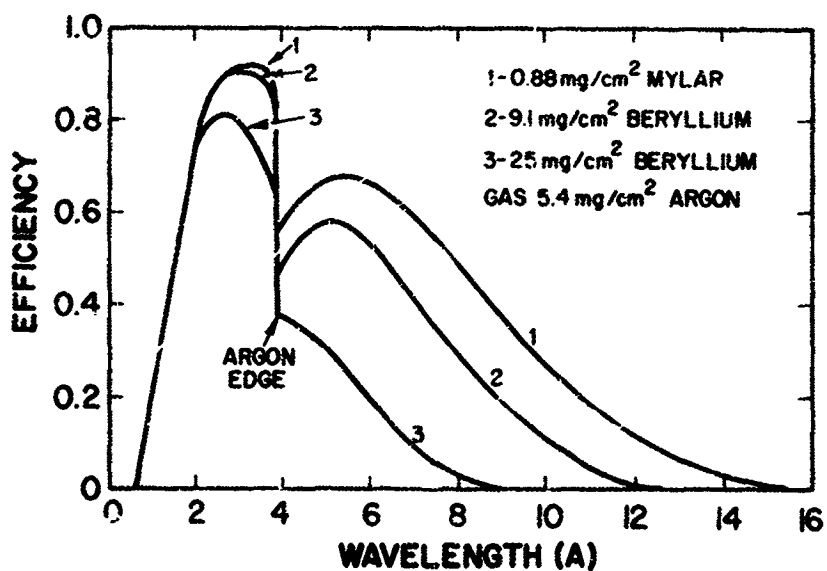


Fig. 5 Calculated efficiency of gas counters with argon filling and different windows.

effect of the photons in the gas, and on the cascade multiplication of the ions produced by these electrons. The counters must be provided with windows thin enough to let X-rays through, yet sufficiently strong to withstand the gas pressure. The efficiency of a counter, ξ , is the product of the probability for an X-ray photon to traverse the window, times the probability for the photon to be absorbed in the gas. It is thus given by the equation:

$$\xi(\lambda) = e^{-\mu_w x_w} (1 - e^{-\mu_g x_g}) \quad (1)$$

where μ_w and μ_g are the absorption coefficients of the window and the gas, x_w and x_g the respective thicknesses. Since μ_w and μ_g depend strongly on wavelength λ , ξ is also a function of λ ; in fact, ξ is appreciably different from zero only within a certain range of wavelengths, which depends on the atomic number and on the thickness of the window and of the gas. The long wavelength limit of the sensitive region is determined by the window becoming opaque and the short wavelength limit by the gas becoming transparent. Thus, a thin, low-Z window and a low Z gas filling will tend to make the counter preferentially sensitive to long wavelengths; with a comparatively thick window and a high-Z gas filling, on the other hand, the counter will discriminate in favor of short wavelengths. Examples of efficiency functions for gas counters with argon filling and different windows appear in Fig. 5.

The lower limit on the window thickness of a gas counter is set by the practical problem of achieving a gas-tight seal. If one insists on this requirement, it is difficult to extend the upper limit of the sensitivity range beyond about 10A, although the transmission curves of certain materials

have "windows" at somewhat longer wavelengths (e.g., aluminum has a "window" from 8A to about 15A).

The long wavelength limit may be extended by relaxing the requirement that the window be gas tight. Although very thin windows (less than several hundred micrograms/cm²) invariably leak, a gas reservoir and pressure regulator may hold the gas pressure in the counter constant within a few percent for the short period of a rocket flight. This is essential because the gas multiplication factor is very sensitive to pressure.

By a suitable choice of voltage between the case and the wires, a gas counter may be operated as a Geiger counter or as a proportional counter (the first mode of operation requiring a higher voltage than the second). As a Geiger counter, the detector gives pulses of uniform size, irrespective of the number of ion pairs N produced in the gas. In the proportional counter regime, the size of a pulse is proportional to N . The average value of N , N_{av} , is proportional to the energy dissipated in the gas. If the stopping power of the gas is sufficiently large, this energy may be taken as equal to the photon energy $E^{(*)}$ so that we can write:

$$N_{av} = E/E_o \quad (2)$$

(*) When a photon undergoes photoelectric absorption, the photoelectron acquires a kinetic energy equal to the photon energy minus the atomic binding energy which may be a substantial fraction of the photon energy. However, most of the binding energy will appear promptly in the form of de-excitation radiation or of kinetic energy of an Auger electron. If the stopping power of the gas is sufficient to absorb all of the electrons and photons emitted subsequent to the process of photoelectric absorption, the energy dissipated in the gas will be practically equal to that of the photon.

where E_0 a characteristic energy dependent on the gas (e.g., $E_0 = 27$ eV for argon). Thus, the pulse height distribution of a proportional counter is directly related to the spectrum of the observed radiation. The counter, however, has a limited spectral resolution, for two separate reasons. In the first place, there may be cases where not all of the energy of the photon which has undergone photoelectric absorption is dissipated in the gas (this effect becomes increasingly important with increasing photon energy). In the second place, the actual value of N corresponding to a given energy dissipation undergoes statistical fluctuations around N_{av} (this effect becomes increasingly important as the photon energy decreases). Note that only if the counter is carefully designed will the multiplication factor remain essentially constant over its sensitive volume.

Examples of actual pulse height distributions obtained with a proportional counter exposed to monoenergetic X-rays of different energies appear in Fig. 6.

With detectors of the type described, ultraviolet rays, cosmic rays and other charged particles of lower energy are possible sources of background. It is easy to protect the detector against ultraviolet rays by a proper choice of the window. In order to reduce the cosmic-ray background, the counters are often set into a well-type scintillation counter whose output pulses are placed in anticoincidence with those of the X-ray counter. Low-energy charged particles, particularly electrons, whose energy is sufficient to traverse the window but not to penetrate the anticoincidence counter cannot be eliminated, and, therefore, represent a source of background that must be taken into consideration.

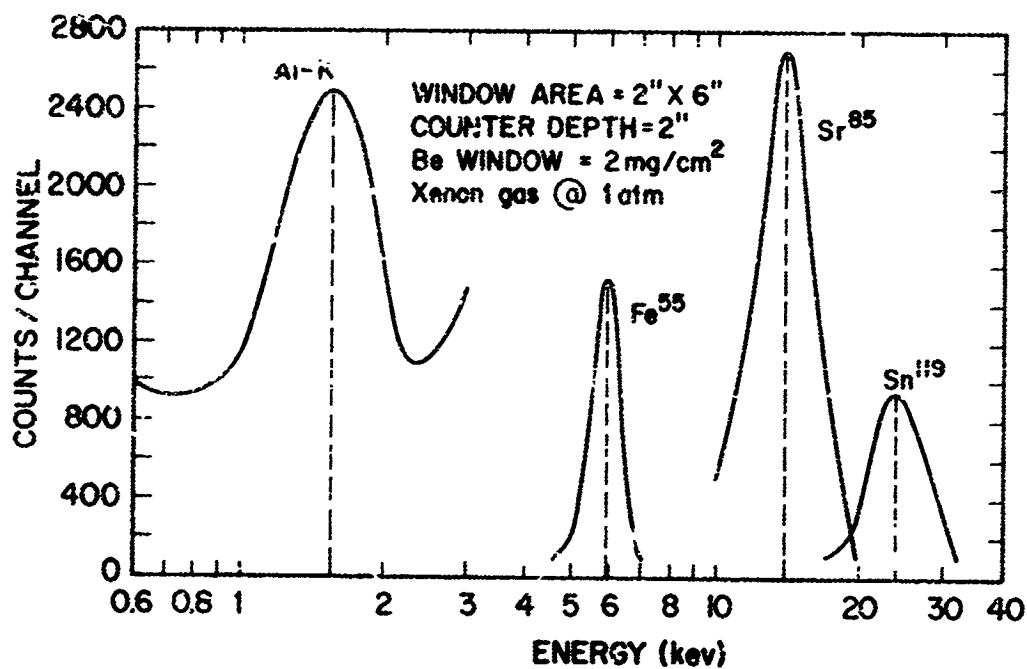


Fig. 6 Pulse-height distributions obtained with a proportional counter exposed to mono-energetic X-rays generated by K-capture (i.e., Sr⁸⁵), isomeric transition (Sm¹¹⁹) and K-X-rays induced by electron bombardment. (Al).

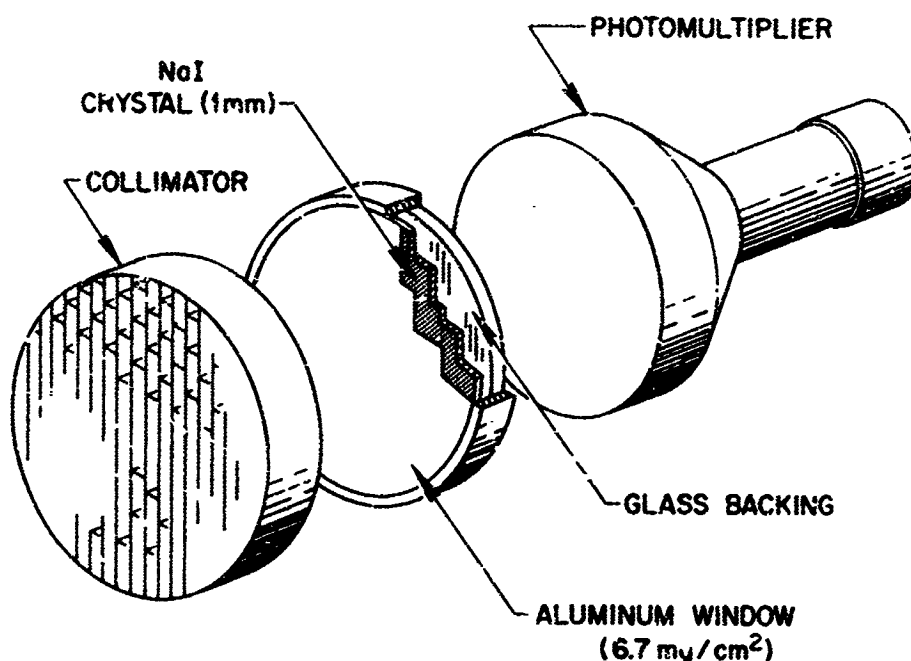


Fig. 7 Schematic drawing of a scintillation counter used for the detection of soft X-rays.

2.1.2 Scintillation Counters

Figure 7 shows, as an example, the design of a scintillation counter used in several rocket experiments. X-ray quanta, incident on the thin slab of scintillating material (e.g. NaI crystal) produce secondary electrons by photoelectric effect. Practically all of these come to rest in the scintillator, giving light pulses proportional to their energy. Some of the photons thus produced reach the photocathode of the photomultiplier, releasing a certain number N of photoelectrons. The photomultiplier output is closely proportional to N .

The efficiency of the detector is the product of two terms. The first is the probability for the X-ray photon to produce a photoelectron in the scintillating material; this probability depends on the thickness and on the atomic number of the scintillator, being high for a high-Z scintillator (such as NaI), and low for a low-Z scintillator (such as anthracene). The second term is the probability that at least one photoelectron be released from the photocathode by the light pulse ($N > 1$). The average pulse height is proportional to the average value of N . It is therefore a linear function of the energy of the X-ray photon, and may be represented by an equation of the type of Eq. (2). In typical situations, the average energy per photoelectron E_0 is of the order of 1000 eV. Comparing this number with the average energy for the production of an ion pair in a gas counter we see that, for a given E , N is smaller for a scintillation counter than for a gas counter. Thus, the smallest detectable photon energy is higher for a scintillation counter than for a gas counter.

The spectral resolution is limited by the fluctuations in the pulse-height corresponding to a given photon energy, which is a decreasing function of N . Therefore, for small values of E , a scintillation counter will not yield as good an energy resolution as may be obtained with a proportional gas counter. For sufficiently high photon energies, on the other hand, scintillation counters have both better efficiency and higher energy resolution than gas counters because of the relatively higher stopping power of the sensitive medium.

A further limitation to the efficiency of scintillation counters for low-energy photons arises from photomultiplier noise. Under optimum conditions, scintillation counters can detect photons down to about 1 keV energy. Because of additional difficulties arising from the requirement of a large sensitive area, until now scintillation counters have been used in X-ray astronomy only in the energy region above 10 keV.

Scintillation counters must be covered with thin films of opaque material to protect the photomultipliers from visible or ultraviolet light. Cosmic-rays and other high-energy particles produce pulses of greater size than X-ray photons, and, therefore, can be easily distinguished from them. Low-energy particles, in particular electrons, cannot be distinguished from X-ray photons on the same basis. However, it is possible to separate these particles from X-rays by comparing the counting rates of two detectors with scintillation crystals of the same mass per cm^2 but different Z (e.g., NaI and anthracene). Such counters have nearly the same response for electrons, but the low- Z counter is practically insensitive to photons.

2.1.3 Photoelectric Detectors

Gas counters cannot be operated in a vacuum without a window and each window places a low-energy limit to the observable portion of the X-ray spectrum. The photoelectric detector does not need a window

and can, therefore, be used to extend the measurements to lower photon energies than are accessible to gas counters.

The possibility of building a photoelectric detector for X-rays rests on the fact, discovered by a group of Russian scientists in 1960,⁽⁶⁾ that several alkali halides have an anomalously high photoelectric yield for X-rays. The design of a photoelectric detector for X-ray astronomy built by the AS&E group is shown in Fig. 8. The photocathode is an evaporated layer of KCl or CsI deposited on a spherical surface. The electrons ejected from the photocathode are focused on the first dynode of an electron multiplier, whose output pulse is proportional to the number of these electrons. The sensitive area of this particular instrument is 40 cm^2 . Its measured efficiency ranges from about 8% for 5 keV photons to about 25% for 0.8 keV photons. Although the instrument may be operated without a window in the high vacuum found at the altitudes where the measurements are made, a filter may be necessary to absorb ultraviolet light. Furthermore, such a window is needed to exclude ambient ionospheric electrons. Several hundred angstroms of aluminum evaporated on a thin organic film will achieve these purposes while allowing the transmission of X-rays well beyond the K-edge of carbon at 44Å. Rejection of visible light does not present a serious problem because of the high work function of KCl or of CsI.

Detectors of this kind have already been flown. Although the results obtained so far are only of a preliminary character, they show that photoelectric detectors hold great promise for the future of X-ray astronomy.

2.2 Collimators

2.2.1 Cellular Collimators

In order to obtain accurate information on the location of the X-ray sources and on their angular sizes, it is necessary to limit the

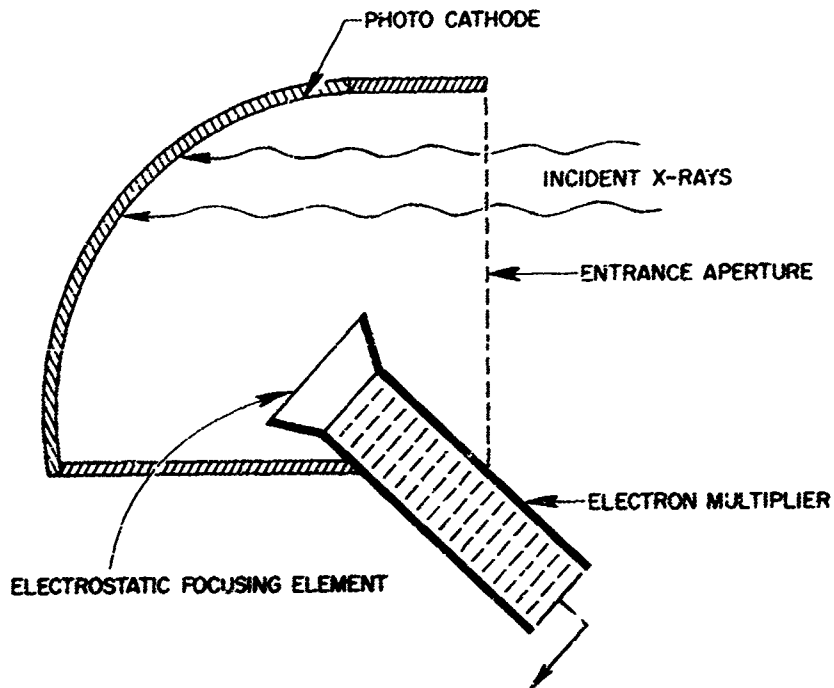


Fig. 8 Schematic diagram of a photoelectric detector for soft X-rays.

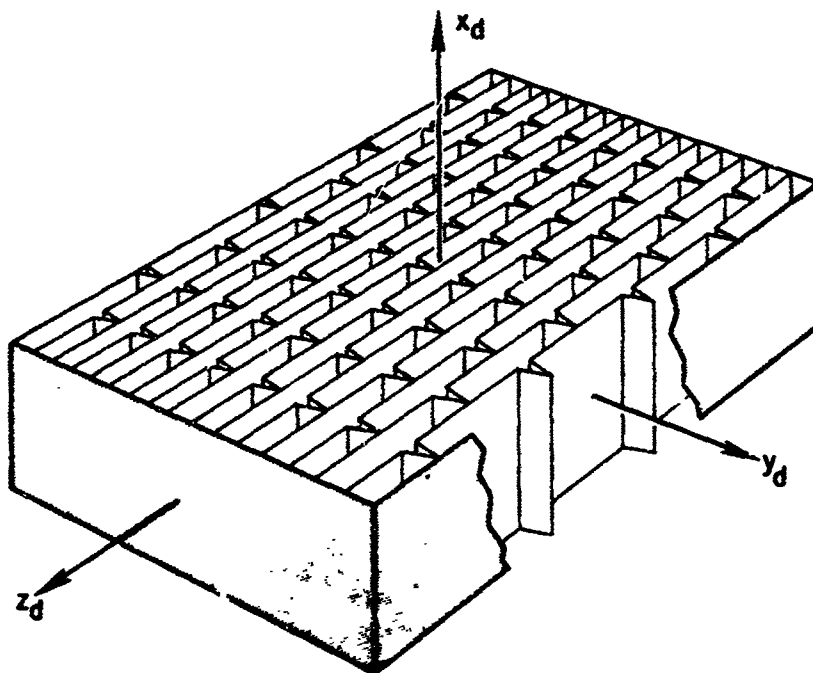


Fig. 9 Schematic drawing of a cellular collimator.

field of view of the detectors by means of suitable collimators. Because of the large area of the detectors and of the limited space available, cellular type collimators have been used such as that shown in Fig. 9. With these collimators one can obtain fields of view of different shapes and different angular widths down to about two degrees. The transmission, of course, is a maximum for a beam parallel to the axis of the collimator (i.e., the normal x_d to its plane; see Fig. 9). The response curves (i.e. the curves giving transmission as a function of angle of incidence in planes containing the collimator axis) have typically nearly triangular shapes. As an example, Fig. 10 shows the computed and the experimental response curves in the plane $x_d y_d$ of a collimator of the type shown in Fig. 9.

2.2.2 Modulation Collimators

In order to improve the angular resolution of a cellular collimator, it is necessary to decrease its field of view. In this manner, however, one also decreases the number of counts recorded when the X-ray source passes across the field of view, and therefore one reduces the statistical accuracy of the data. There is thus a practical limit to the resolution that may be obtained with these devices when used on spinning rockets.

A collimator of a different type, which combines high resolution with wide field of view was conceived by M. Oda⁽⁷⁾ and has been developed by the ASE-MIT group. Known as the "modulation collimator", it consists essentially of two plane grids of parallel wires placed one in front of the other at a suitable distance (Fig. 11). The diameter of the wires, d , is nearly equal to the spacing between adjacent wires, s . In a parallel beam

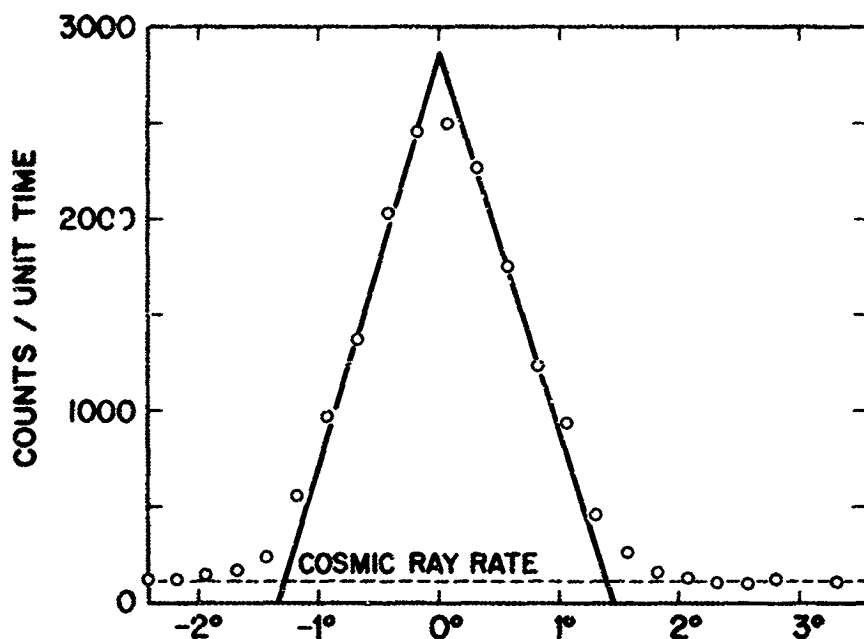


Fig. 10 Experimental response curve of a cellular collimator to X-rays (circles) compared with its computed response function (solid line). The angular divergence of the X-ray beam was less than $1/2^\circ$. The X-ray beam was in the (\hat{x}_d, \hat{y}_d) plane (Fig. 9) and the abscissa represents the angle formed by this beam with the normal to the collimator (\hat{x}_d) .

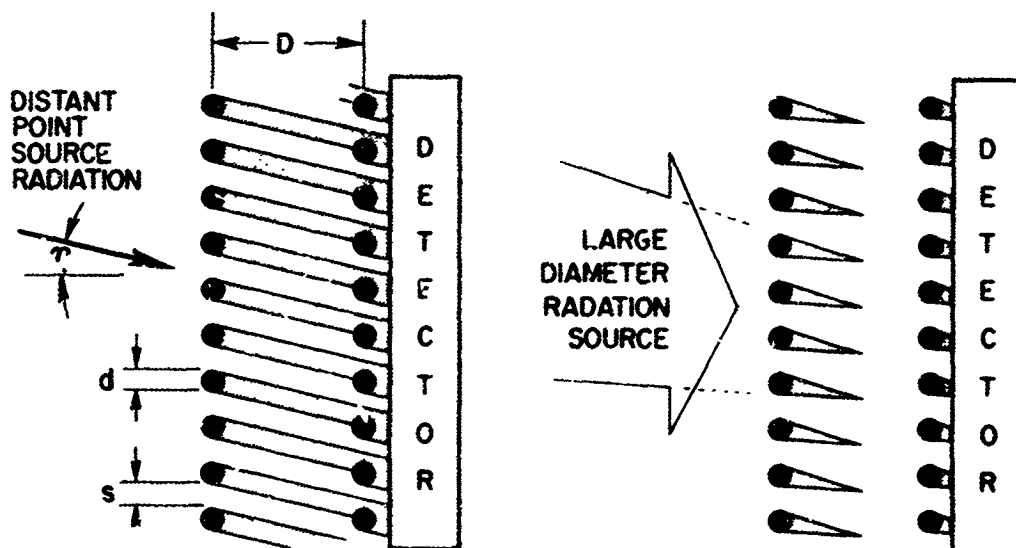


Fig. 11 Illustrating the principle of operation of the modulation collimator. The drawing on the left indicates the shadowing that obtains with parallel radiation.

of rays, the front grid casts a shadow on the rear grid. The shadow shifts as the orientation of the collimator relative to that of the incident beam changes, and the transmission of the collimator changes correspondingly, being a maximum when the shadow of the front wires falls exactly on the back wires, and a minimum when it is centered between adjacent wires.

Figure 12 shows the computed response curve of a modulation collimator in a plane perpendicular to the wires in the case of a parallel beam coming from a distant point source. The abscissa is the angle η between the beam and the collimator's axis (i.e. the normal to the planes of the grids; see Fig. 11). The ordinate is the transmission. The distance D between the grids is large compared with the distance $d + s$ between the axes of adjacent wires. For small values of η the angular distance between maxima is:

$$\Delta \eta : (d + s)/D$$

It is clear that a distant source with angular dimensions δ small compared with $\Delta \eta$ will produce practically the same pattern of maxima and minima as a point source. If, on the other hand, the source has angular dimensions large compared with $\Delta \eta$ no "modulation" of the transmitted intensity will occur as the angle of incidence varies. With a source of angular dimensions comparable to $\Delta \eta$, a variation of the angle of incidence will produce a partial modulation, from which it may be possible to estimate the actual angular size of the source in the direction perpendicular to the wires. The minimum angular size of a source that can be distinguished from a point source depends on the mechanical precision achieved in the construction of the collimator, on the statistical accuracy of the data and on the contribution

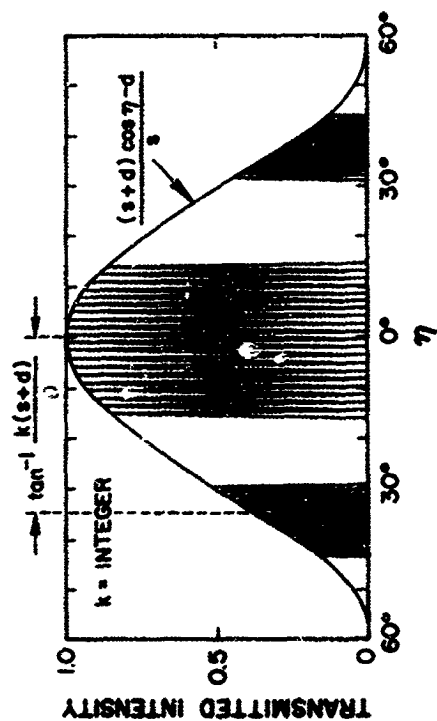


Fig. 12 Calculated angular response of a modulation collimator. The X-ray beam lies in the plane perpendicular to the grids (\hat{x}_d, \hat{y}_d plane), the abscissa is the angle η formed by the beam with the normal to the grids.

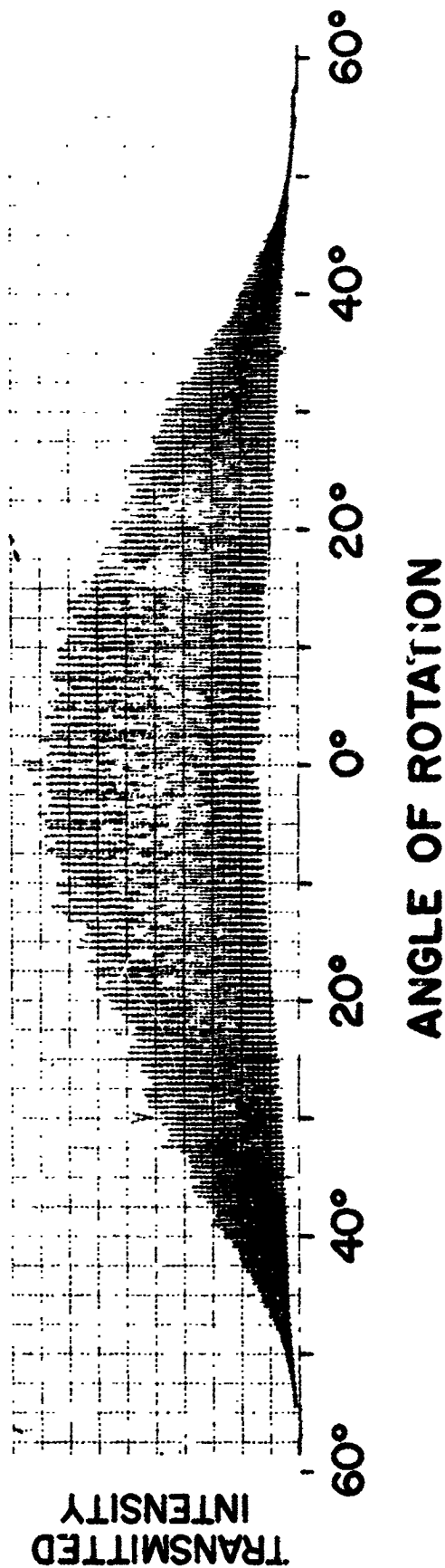


Fig. 13 Angular response of modulation collimator measured with visible light. The abscissa is the angle η (Fig. 11). Dimensions of the collimator are shown.

of the diffuse background radiation to the measured fluxes. The experience with the collimators that have been used has shown that this minimum size is about a quarter of $\Delta \eta$.

Modulation collimators with $\Delta \eta$ as small as 8 arc minutes have been used. Figure 13 shows the response curve of a modulation collimator with $\Delta \eta$ of about 32 arc minutes, measured with visible light; Fig. 14 shows a similar curve for a modulation collimator having a $\Delta \eta$ of 2 degrees, measured with X-rays.

2.3 Image Forming Telescopes

It seems difficult to obtain resolving powers substantially better than several arc seconds by means of modulation collimators such as those described above. Moreover, these devices give ambiguous results when several sources are within their field of view. In order to improve the resolution further and to investigate the actual structure of an extended source, instruments of a different type are needed. The ideal instrument is an image-forming telescope. It is actually possible to build telescopes for X-rays using the phenomenon of total external reflection of X-rays under grazing incidence.^(8, 9) It can be shown that two reflections are needed to obtain an image. The two reflecting surfaces may be a paraboloid and an hyperboloid with its external focal point at the focal point of the paraboloid, such as shown schematically in Fig. 15. Other combinations of surfaces, however, are possible.

Image forming telescopes have been used so far only for solar X-ray astronomy. Figure 16 is the photograph of one such instrument. In Fig. 17 a picture of the Sun in X-rays obtained with this telescope from a rocket⁽¹⁰⁾ is compared with a picture of the Sun in $\text{Li}\alpha$ obtained almost simultaneously

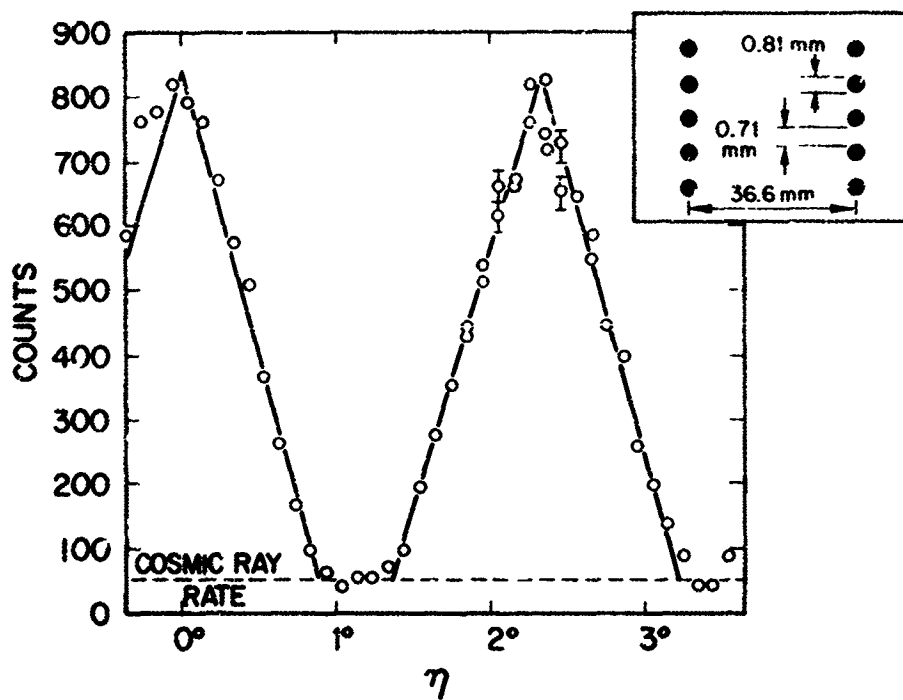


Fig. 14 Angular response of modulation collimator measured with X-rays. The abscissa is the angle η (Fig. 11).

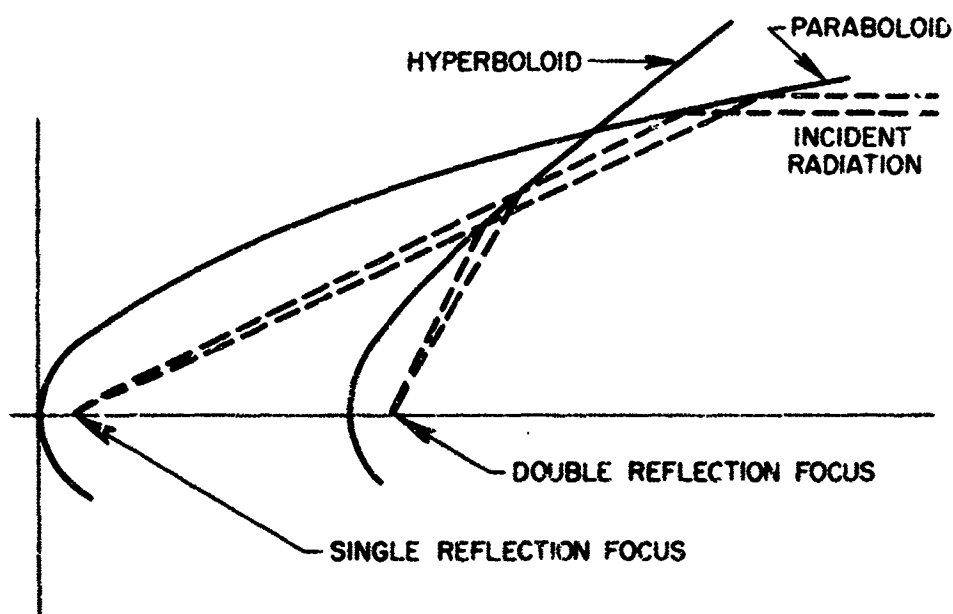


Fig. 15 Ray tracing in a grazing-incidence X-ray telescope. The focus of the paraboloid coincides with the external focus of the hyperboloid.

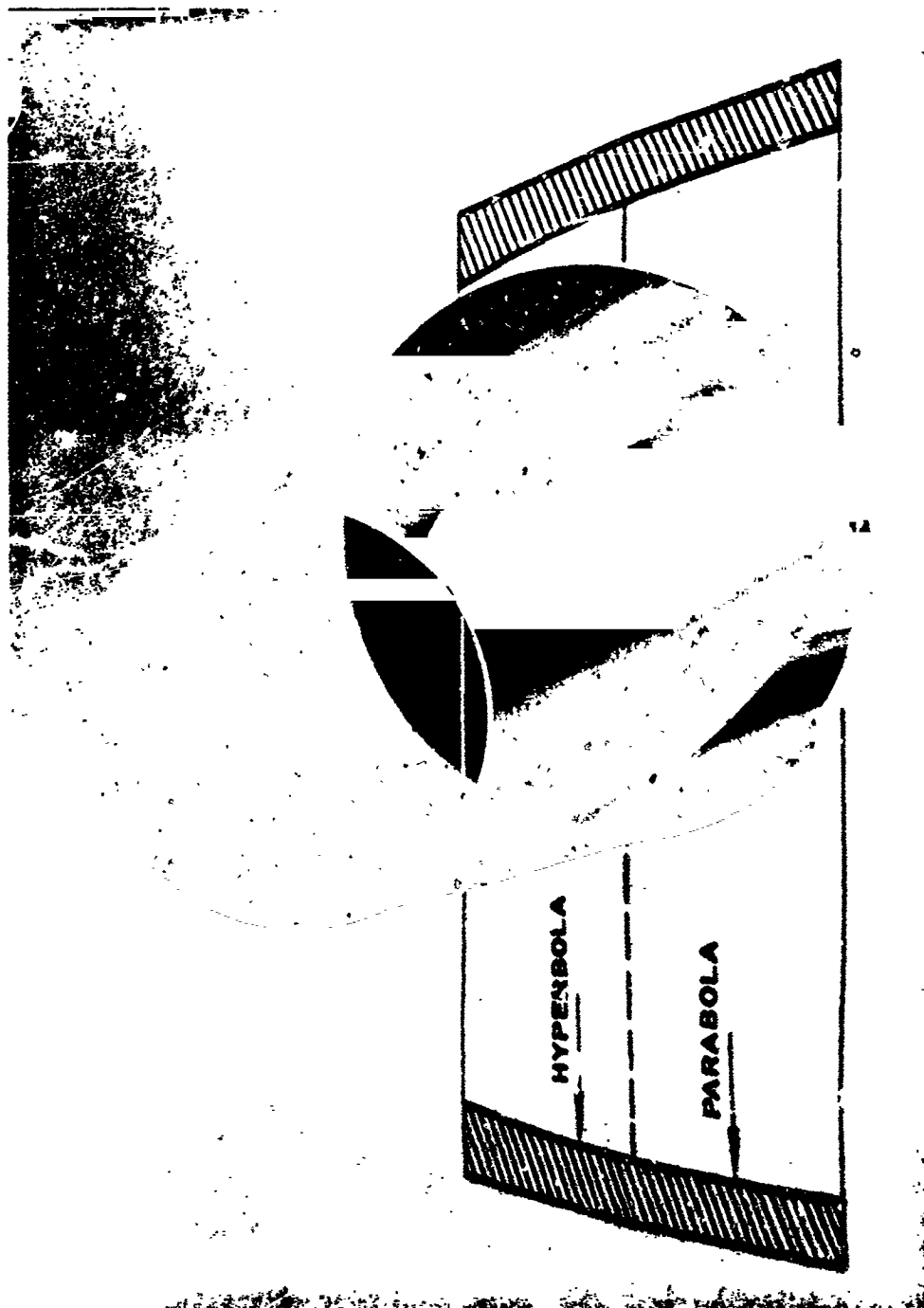
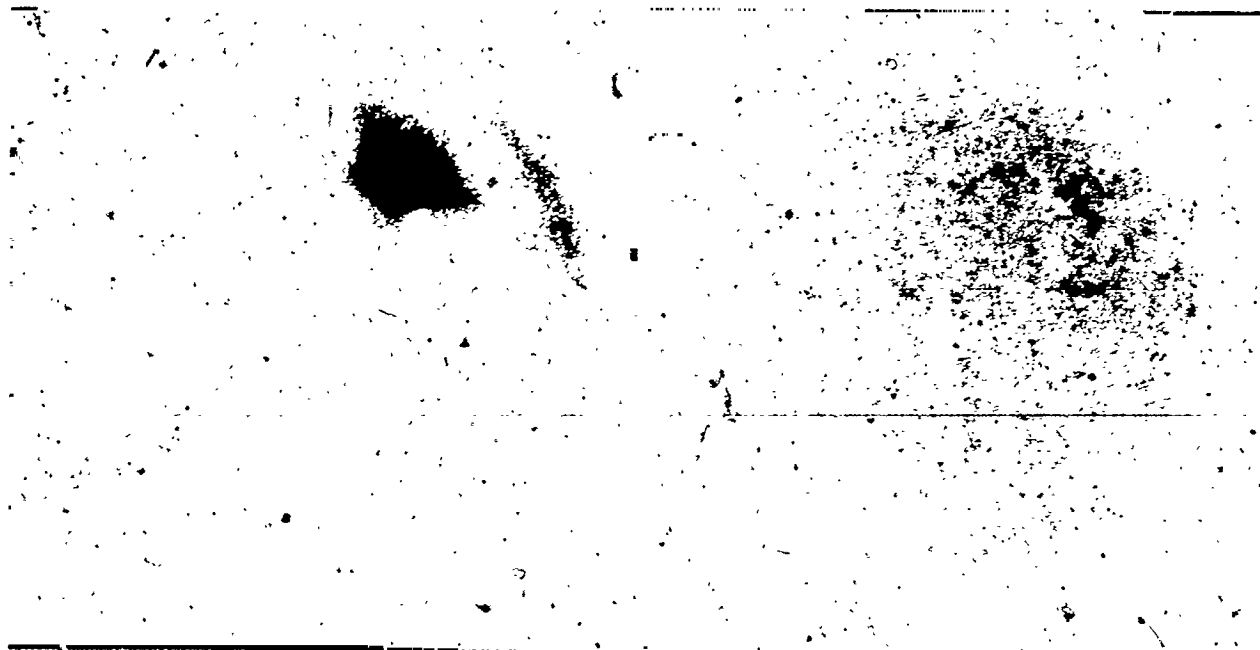


Fig. 16 Photograph of a focusing X-ray telescope superimposed on the drawing of a section of the interior surfaces.



X-Ray photograph of Sun
17 March 1965, 1510-1515 hrs. U. T. WSMR
106 sec exposure
0.15 mil mylar filter (2200 Å Al)
Ilford Industrial G film

H α
17 March 1965, 1520 hrs. U. T.
(by courtesy of Sacramento Peak Observatory,
Air Force Cambridge Research Laboratory)

Fig. 17 Photographs of the Sun in X-rays and in H α . X-ray photograph at left was taken during rocket flight, using the focusing telescope shown in Figure 16.

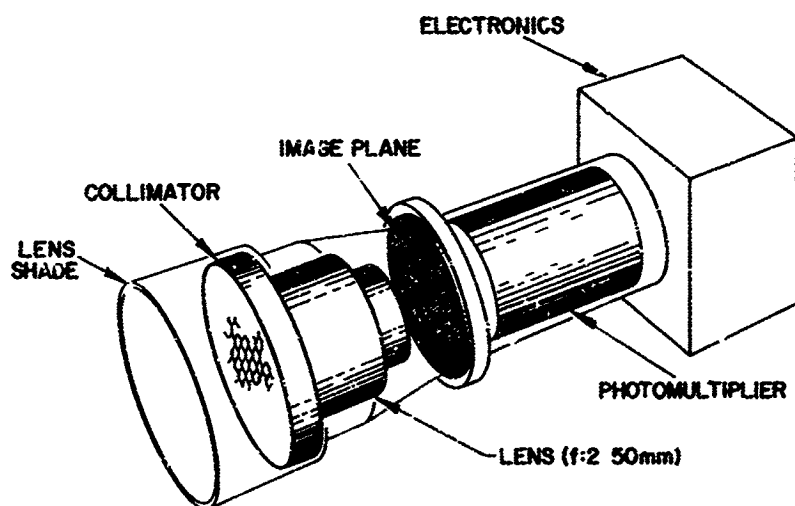


Fig. 18 Schematic drawing of an optical aspect sensor.

with an ordinary telescope from the ground. The use of image forming telescopes for the study of extra solar sources shows great promise.

2.4 Optical Sensors

In order to determine the parameters of the vehicle's rotational motion during the period of observation, one generally uses optical sensors , capable of detecting celestial objects such as the Sun, the Moon and the stars. An example of such an instrument is shown in Fig. 18. It consists essentially of an objective lens with a rectangular slit in its focal plane and a photocell behind it. This arrangement provides a "rectangular" response function as defined by the slit in the focal plane.

3.0 ANALYSIS PROBLEMS RELATIVE TO ROCKET OBSERVATIONS

Both freely spinning rockets and attitude controlled rockets have been used for X-ray observations. In the first instance, if the rocket behaves like a rigid body and external torques are negligible, its rotational motion consists of a spin (with constant angular velocity ω_s) around the minor axis of inertia, accompanied by a precession (with constant angular velocity ω_p) of the spin axis around an axis fixed in space and parallel to the total angular momentum (precession axis). The minor axis of inertia is practically coincident with the longitudinal axis of the rocket whose momental ellipsoid may be regarded as a surface of revolution around this axis. The half-apex angle of the precession cone, α , is related to ω_s and ω_p by the equation:

$$\cos \alpha = \frac{\omega_s}{\omega_p} = \frac{I_1}{I_2 - I_1} \quad (3)$$

where I_1 and I_2 are the moments of inertia relative to the spin axis and to a direction perpendicular to it. In the most accurate observations, it becomes necessary to take into account the possibility that the actual rotational motion of the rocket may differ slightly from that described above. The deviations occur mainly not because of the presence of external torques, but because the rocket does not behave exactly like a rigid body. Therefore, the direction of the precession axis remains fixed in space, but ω_s , ω_p and α may undergo small and gradual changes during the time of observation.

Useful X-ray observations may be made only above 80 km. The rockets that have been used (Aerobee) usually reach a maximum altitude somewhat in excess of 200 km, which gives an observation time of about 5 minutes. During boost the rocket is spun up to two revolutions per second for the purpose of stabilization. If it is not purposely despin, the rocket will maintain approximately this spin frequency until it re-enters the atmosphere (atmospheric friction during the ascent does not reduce the spin frequency substantially). With such high spin frequency, the apex angle of the precession cone is small and $\omega_p \ll \omega_s$.

In some experiments, the spin angular velocity of the rocket is reduced by means of gas jets or a yo-yo despin mechanism after the rocket has traversed the denser part of the atmosphere. The decrease of ω_s results in a widening of the precession cone and, in the extreme case, α may approach 90° .

Actively controlled rockets offer the possibility of exploring selectively predetermined regions of the sky. On the other hand, one cannot use rigid-body dynamics to predict the character of their motion. In the experiments carried out thus far, an attitude control system (or ACS), based on gyroscopes

as sensing devices, is used to control the rocket orientation. By means of gas jets, it is possible to point the axis of any given detector to within several degrees of any given direction in the sky, or to sweep it at a prescribed speed over a prescribed angular interval.

3.1 Frames of Reference

In the analysis of the data and in the presentation of the results obtained with freely spinning rockets, it is convenient to consider a number of different frames of reference. Each shall be defined by a Cartesian coordinate system, specified by three mutually perpendicular unit vectors $\hat{x}, \hat{y}, \hat{z}$. We shall call x, y, z the three coordinates of the unit vector \hat{r} specifying a given direction. To each Cartesian system, we shall associate a polar system of coordinates ϕ, λ , where ϕ is the azimuth and λ is the elevation. We take the polar axis in the direction of \hat{z} and the plane $\phi = 0$ coincident with the (\hat{x}, \hat{z}) plane.

Thus:

$$\begin{aligned} x &= \cos \phi \cos \lambda \\ y &= \sin \phi \cos \lambda \\ z &= \sin \lambda \end{aligned}$$

A list of the various frame of reference appears below.

(a) Celestial Frame of Reference $\hat{x}_c, \hat{y}_c, \hat{z}_c$; the (\hat{x}_c, \hat{y}_c) plane coincides with the celestial equator (which coincides with the Earth's equator); \hat{z}_c points toward the north pole and \hat{x}_c toward the ascending node of the ecliptic. Thus ϕ_c is the right ascension and λ_c is the declination.

(b) Precession Frame of Reference $\hat{x}_p, \hat{y}_p, \hat{z}_p$; \hat{z}_p is parallel to $\vec{\omega}_p$, i.e. to the axis of the precession cone; \hat{x}_p is parallel to the vector product $\hat{z}_c \times \hat{z}_p$; i.e. it lies in the (\hat{x}_c, \hat{y}_c) plane, and points in the direction of the "ascending node of the precession equator". With respect to

the celestial frame of reference, the precession frame of reference is defined by the right ascension $\phi_c^{(p)}$ and by the declination $\lambda_c^{(p)}$ of the precession axis \hat{z}_p . If angular momentum is conserved, the precession frame of reference is fixed with respect to the celestial frame of reference.

(c) The Spin Frame of Reference $\hat{x}_s, \hat{y}_s, \hat{z}_s$; \hat{z}_s is parallel to $\vec{\omega}_s$, i.e. to the spin axis of the rocket; \hat{x}_s lies in the direction of $\hat{z}_p \times \hat{z}_s$. With respect to the precession frame of reference, the spin frame of reference is defined by the angles $\lambda_p^{(s)}$ and $\phi_p^{(s)}$, which are the elevation and the azimuth of \hat{z}_s as measured in the precession frame of reference, as shown in Fig. 19. If momentum and energy are conserved, $\lambda_p^{(s)}$ is a constant and $\alpha = \frac{\pi}{2} - \lambda_p^{(s)}$ represents the semi-aperture of the precession cone, while $\phi_p^{(s)}$ varies uniformly from 0 to 2π during one precession period.

(d) The Rocket Frame of Reference $\hat{x}_r, \hat{y}_r, \hat{z}_r$; \hat{z}_r coincides with the figure axis of the rocket and \hat{x}_r is fixed with respect to the rocket. If the figure axis coincides with the spin axis then \hat{z}_r coincides with \hat{z}_s . \hat{x}_r rotates relative to \hat{x}_s with angular velocity ω_s , and if ω_s is constant, the azimuth of \hat{x}_r in the spin frame of reference is $\phi_s^{(r)} = \omega_s (t - t_0)$ where t_0 is the time when \hat{x}_r and \hat{x}_s are coincident. In the ASE-MIT experiments so far it has not proven necessary to allow for the possible small discrepancy between the spin and figure axes.

In what follows we shall have occasion to use the equation relating the elevation λ_r of a unit vector \vec{r} in the rocket frame to the elevation λ_p of the same vector in the precession frame and to the relative azimuth, $\phi_p - \phi_p^{(s)}$, of the vector and of the spin axis in the precession frame. This equation may be derived from the vector identity $(\hat{z}_p \times \hat{z}_s) \cdot (\hat{z}_p \times \vec{r}) = \hat{z}_s \cdot \vec{r} - (\hat{z}_s \cdot \hat{z}_p) (\vec{r} \cdot \hat{z}_p)$ and reads:

$$\sin \lambda_r = \sin \lambda_p \cos \alpha + \cos \lambda_p \sin \alpha \cos (\phi_p - \phi_p^{(s)}) \quad (4)$$

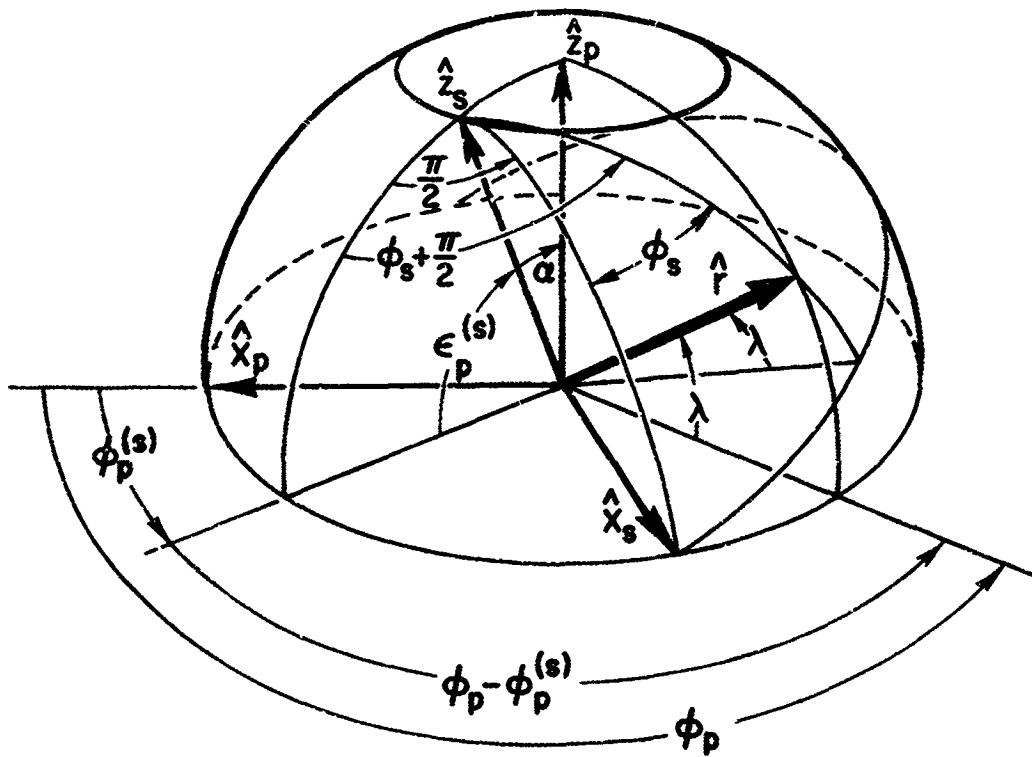


Fig. 19 Precession and spin coordinate systems.

The above equation shows that if \vec{r} is fixed in the precession frame, λ_r varies from $\lambda_p + \alpha$ to $\lambda_p - \alpha$ during a precession cycle. Note that if λ_p and α are small angles, Eq. (4) may be approximated by:

$$\lambda_r \approx \lambda_p + \alpha \cos (\Phi_p - \Phi_p^{(s)}) \quad (5)$$

3.2 Freely Spinning Rockets

Consider now a freely spinning rocket carrying a detector (X-ray counter or optical sensor). Suppose that the detector's axis forms an angle $\lambda_r^{(d)} = \lambda_s^{(d)}$ with the equatorial plane of the rocket. Then its elevation in the precession frame will oscillate between $\lambda_r^{(d)} - \alpha$ and $\lambda_r^{(d)} + \alpha$ during each spin. On a rectangular grid (plate Carree projection) its representative point will describe a nearly sinusoidal curve with an amplitude equal to α and a phase that changes gradually from one spin to the next (see Fig. 20). Thus the region of the sky explored by the detector becomes wider as the apex angle of the precession axis increases.

In the rocket's frame of reference, on the other hand, the detector's axis is fixed, while the vector pointing to a celestial object moves in azimuth with slightly varying angular velocity, while changing its elevation between $\lambda_p^{(o)} - \alpha$ and $\lambda_p^{(o)} + \alpha$ during the precession cycle. On a rectangular grid, the representative point of the celestial object moves along a nearly horizontal line, which oscillates up and down filling the band between $\lambda_p^{(o)} - \alpha$ and $\lambda_p^{(o)} + \alpha$ (see Fig. 21). The object will be seen by a given detector if the latter's field of view overlaps this band.

(a) Despun rockets with long spin periods (~ 5 sec), long precession periods (~ 300 sec), and large precession cone angles

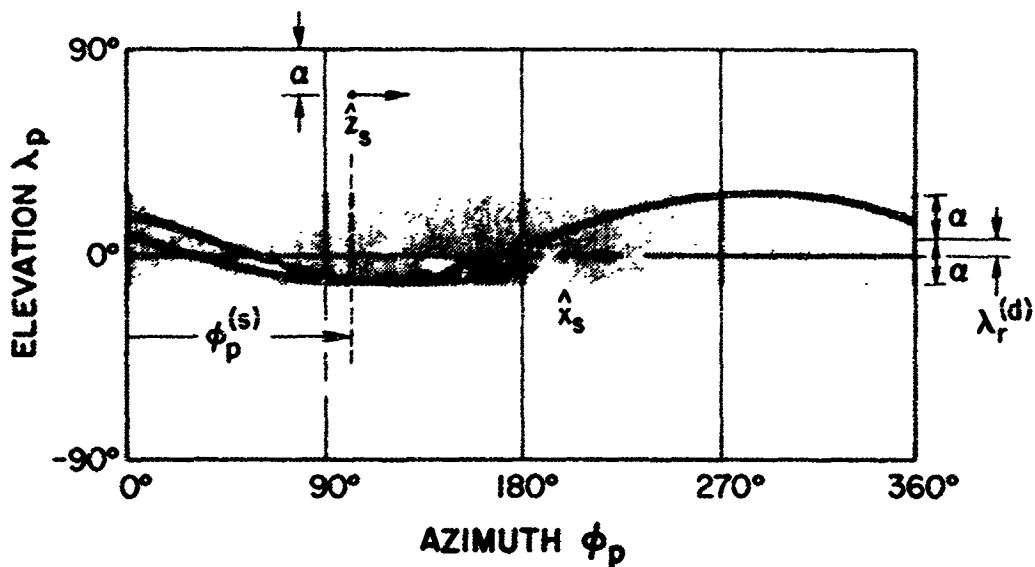


Fig. 20 Motion of detector axis in the precession frame of reference. Shaded region represents the band covered by the detector axis during an entire precession cycle. The solid curve within the shaded region is the path of the detector axis during about 1.5 spin periods. The short arrow at z indicates the motion of the rocket axis during the same time. $\lambda_r(d)$ is the elevation angle of the detector axis in the rocket frame of reference.

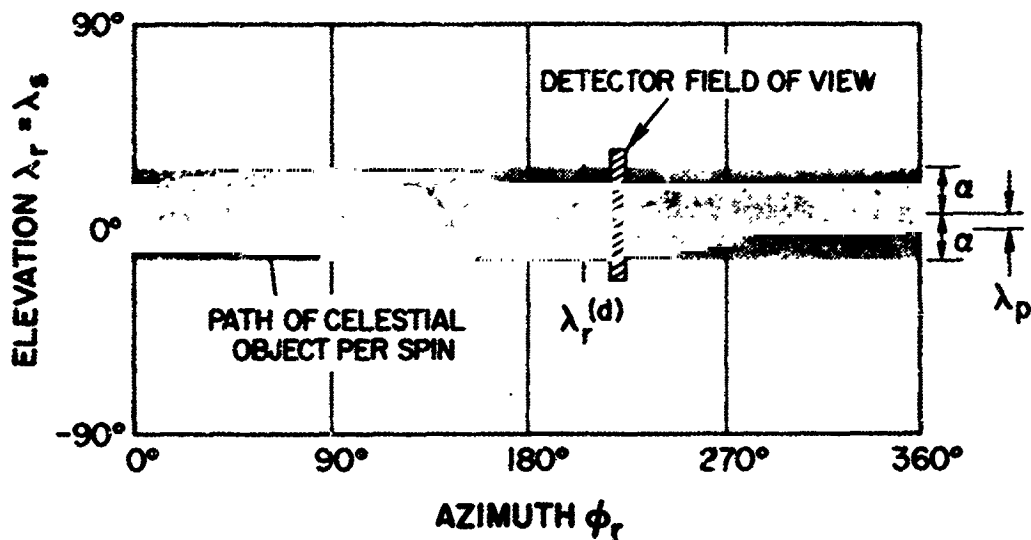


Fig. 21 Motion of a celestial object in the rocket frame of reference. Shaded portion is the region traversed by a given celestial object during the precession cycle and the solid line is the motion of the object during slightly more than one spin period.

($\alpha \gtrsim 60^\circ$) have been employed in the NRL experiments. The nearly sinusoidal curve traced out by the representative point of the axis of a detector carried on such a flight changes in phase by a substantial amount during each spin. Thus any source within the large region of explored sky is detected on only a few successive spins out of the entire flight. In analyzing the X-ray data from such an experiment, one searches for evidence of significant variations in the counting rate. These may show periodicities extending over several spins if the detector's field of view is large enough so that the regions swept out in successive spins overlap one another. The celestial orientations of the detector's axis when the maximum rates are recorded is, of course, established by reference to the data obtained by optical and magnetic sensors. If the field of view has a nearly circular shape, then it is possible to estimate a source's position making use of the fact that the number of counts produced by the source during one spin is a decreasing function of the minimum angular distance between the detector's axis and the source during that spin. By plotting the numbers of counts as a function of this distance, and comparing the curve thus obtained with the known angular response of the collimator, one can also evaluate the angular diameter of the source, or place an upper limit to it. Obviously the accuracy of both the position and size determinations will depend on the statistical accuracy of the data (and, therefore, on the area of the detector) as well as on the angular aperture of the collimator.

(b) A situation of a somewhat different character occurs in experiments like those of the ASE-MIT group, which have employed rockets that retain their relatively high initial spin rates ($\sim 2 \text{ sec}^{-1}$), have small precession cone angles ($\alpha \lesssim 10^\circ$), and have precession periods that are

sufficiently short so that several complete precession cycles occur during the period of observation. In these experiments a source within the relatively small region of sky scanned by a given detector is detected on many successive spins during those portions of the several precession cycles when the elevation of the source lies within the sensitive range of the detector. In order to exploit the information about a source which is potentially available in the data it is necessary to combine the data from many spins, taking proper account of the effect of the precession motion on the periodicity. A source too weak to have a statistically significant effect on the counting rate during one spin may be detected in the combined data from many spins. From such data it is possible to obtain precise information on the sizes and locations of sources.

In order to deal with the complications caused by precession motion in the analysis of data obtained from fast and freely spinning rockets, we have found it convenient to introduce a special angular variable ψ which we call the bearing. This angle is defined by the equation

$$\psi = \phi_s + \phi_p^{(s)} + \pi/2$$

where ϕ_s is the azimuth of a given direction in the spin frame, and $\phi_p^{(s)}$ is the azimuth of the spin axis in the precession frame. If the given direction is fixed in the rocket frame, as are the directions of the axes of the various detectors, then we have $\dot{\phi}_s + \dot{\phi}_p^{(s)} = \omega_s + \omega_p$. Thus the bearing angle $\psi^{(d)}$ of a detector's axis at any given instant may be expressed as a function of time by the equation

$$\psi^{(d)} = \int_0^t (\omega_s + \omega_p) dt + \psi_0^{(d)}$$

where $\psi_0^{(d)}$ is the bearing angle at $t = 0$. If the given direction is that of

a celestial object (which is, of course, fixed in the precession frame) then during each precession cycle $\phi_p^{(s)}$ increases uniformly by 2π while $\phi_s^{(o)}$, the spin azimuth of the object, decreases non-uniformly by 2π . Thus the bearing angle of the object $\psi^{(o)}$ varies about an average value which is, in fact, the precession azimuth of the object, i.e.

$$\psi_{av}^{(o)} = \phi_p^{(o)}$$

This is obviously true in the limit $\alpha = 0$ where $\phi_p^{(o)} = \phi_p^{(s)} + \pi/2 + \phi_s^{(o)}$ as can be seen in Figure 19. In this case we have

$$\psi^{(o)} = \phi_p^{(o)}$$

In the general case when $\alpha \neq 0$, one can show that the difference $\psi^{(o)} - \phi_p^{(o)}$ is an antisymmetric function of the difference $\phi_p^{(o)} - \phi_p^{(s)}$. Since $\psi^{(o)} = \phi_p^{(o)}$ when this difference is zero (or π), the average value must be equal to $\phi_p^{(o)}$ as previously stated.

Under the assumption of a rigid, freely-spinning rocket, $(\omega_s + \omega_p)$ is a constant so that the bearing angle of a detector's axis, $\psi^{(d)}$, increases linearly by 2π during a time interval equal to $2\pi/(\omega_s + \omega_p)$. The transit times of a celestial object through the meridian plane of a detector are determined by the intersections of the heavy solid curve, representing the time dependence of the bearing angle $\psi^{(o)}$ of a celestial object, with the saw-tooth solid line representing the time variation of the bearing angle $\psi^{(d)}$ of the detector's axis (see Fig. 22).

The explicit expression for the bearing angle of a given unit vector \vec{r} fixed in the precession frame in terms of α and $\phi_p^{(s)}$ is rather cumbersome. It may be expressed implicitly, however, in the following way which is particularly well suited to computer calculations. The components r_{si} in

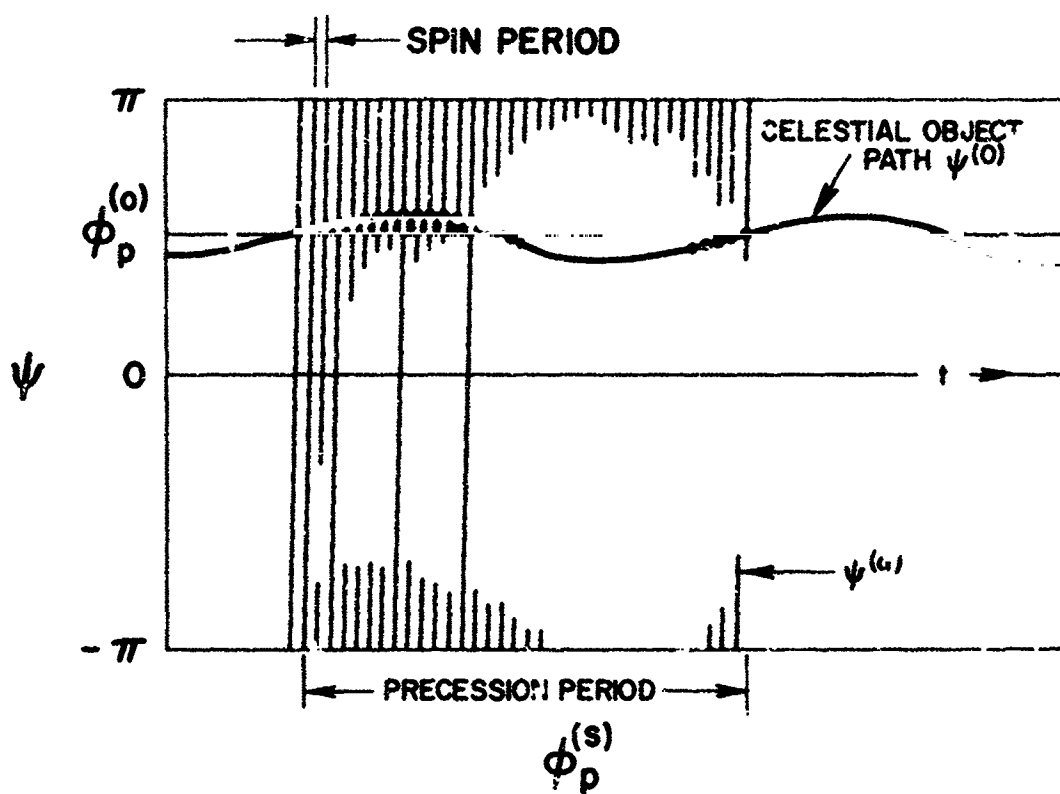


Fig. 22 Time variation of the bearing angle of a celestial object (heavy solid line) and of the X-ray detector axis (light solid line) during several precession cycles. Average bearing angle of the object is its precession azimuth $\phi_p^{(o)}$.

the spin. frame are related to the components r_{pk} in the precession frame by the matrix equation

$$r_{si} = T_{ij}^{(2)} T_{jk}^{(1)} r_{pk}$$

where

$$r_{pk} = \begin{vmatrix} (\cos \lambda_p \cos \phi_p) \\ (\cos \lambda_p \sin \phi_p) \\ (\sin \lambda_p) \end{vmatrix}$$

$$T_{jk}^{(1)} = \begin{vmatrix} [\cos(\phi_p^{(s)} + \pi/2)] & [\sin(\phi_p^{(s)} + \pi/2)] & 0 \\ [-\sin(\phi_p^{(s)} + \pi/2)] & [\cos(\phi_p^{(s)} + \pi/2)] & 0 \\ 0 & 0 & 1 \end{vmatrix}$$

$$T_{ij}^{(2)} = \begin{vmatrix} 1 & 0 & 0 \\ 0 & \cos \alpha & \sin \alpha \\ 0 & -\sin \alpha & \cos \alpha \end{vmatrix}$$

The orthogonal transformation matrices $T_{jk}^{(1)}$ and $T_{ij}^{(2)}$ correspond to the two rotations required to bring the precession frame into coincidence with the spin frame, namely, a positive rotation by the angle $\phi_p + \pi/2$ about the \hat{z}_p axis, followed by a positive rotation by the angle α about the \hat{x}_s axis. The bearing angle can be expressed in terms of the transformed components of \vec{r} by the equation

$$\psi^{(c)} = \frac{r_{s2}}{|r_{s2}|} \arccos(r_{s1} / \sqrt{r_{s1}^2 + r_{s2}^2}) + \phi_p^{(s)} + \pi/2.$$

Turning now to the actual analysis of the data, the first step is to find an approximate value for $\omega_p + \omega_s$, the bearing angular velocity, of the detector axes. To do this we search for a sequence of nearly periodic signals from one of the sensors (optical, X-ray or magnetic). The average value of the interval between successive signals in a sequence divided into 2π is then used as the first approximation to $\omega_p + \omega_s$.

The second step is the computation of the values of the bearing $\psi^{(d)}$ relative to the bearing $\psi_0^{(d)}$ at some given arbitrary time of the detector axis at the instants when signals were observed. This is done using the formula

$$\psi^{(d)} - \psi_0^{(d)} = \int_{t_0}^t (\omega_s + \omega_p) dt$$

with $\omega_s + \omega_p$ initially taken as constant and equal to the approximate value of this quantity determined as described above. In order to obtain a second approximation to $\omega_p + \omega_s$ we construct a plot in which each signal is indicated by a mark with the coordinates $(\psi^{(d)} - \psi_0^{(d)}, t)$. Recurrent signals from a celestial object give rise to a trail of marks advancing in t , and drifting gradually one way or another in $\psi^{(d)} - \psi_0^{(d)}$, depending on the error in $\omega_s + \omega_p$. From the trends revealed by this plot we determine an improved value of $\omega_s + \omega_p$ which reduces the long term drift in the relative bearing. It turns out, however, that sounding rockets with liquid fuels are not perfectly rigid bodies after cutoff. Thus $\omega_s + \omega_p$ generally varies significantly during an experiment. To allow for this we express $\omega_s + \omega_p$ as a power series in t in the form

$$\omega_s + \omega_p = \omega_0 + At + Bt^2 + \dots$$

In practice we have found it necessary to use only the first order term in t in order to eliminate nearly all long term drift.

Of course, even after correcting the computation of the relative bearing for the long term drift of $\omega_s + \omega_p$, there remain the periodic variations in the relative bearing of a fixed source due to the precession motion. This motion, as we have seen, causes the bearing of the source to vary around its average value (which is its precession azimuth). A plot of the frequency of signals versus the relative bearing of the detector's axis will therefore show a peak whose width is greater than the spread due to the azimuthal angular resolution of the detector and the angular width of the source itself. At this point the periodic precession variation of $\psi^{(o)}$ as well as any residual long term drift in $\omega_s + \omega_p$ can be compensated by adding an empirically determined and smoothly varying quantity to the calculated values of $\psi^{(d)}$. A plot of this compensated quantity, which is essentially $\psi^{(d)} - \psi^{(o)}$, will now show a peak whose width is as narrow as the limit set by the resolution of the detector and the angular width of the object. When this method, which we call "self-synchronization", was applied to the ScoX-1 peak in Figure 29, the width of the modified peak was found to be consistent with the assumption that the angular width of ScoX-1 is less than 20 arc minutes.

It is worth noting that the average over an integral number of precession cycles of the bearing of the signals in a peak is a correct measure of the precession azimuth of the corresponding celestial object even if the object passes in and out of the detector's elevation range. This is true because the deviation of $\psi^{(o)}$ from $\phi_p^{(o)}$ when the object crosses a given rocket elevation in one direction is just the negative of the deviation when it crosses in the other direction. Thus the average relative bearing of the object during the time when it is within the detector's elevation range, plus the phase $\psi_o^{(d)}$, which is yet to be determined, is, in fact, the precession azimuth of the object.

The third step in the analysis is the determination of the precession motion and the orientation of the precession axis in the celestial frame of reference. The celestial orientation of the precession frame of reference is determined from the star sensor data. These data consist of the transit times of various stars whose identity is initially unknown. Selecting data from portions of the precession cycle when signals from several stars are observed in each rocket rotation, we determine the relative bearings of the unknown stars. With the aid of a star catalogue and an appropriate computer program we then search for a spin axis direction in the celestial frame which would cause the star sensor to sweep over a combination of stars with relative bearings that match the ones observed. In this way the stars which caused the observed signals are unambiguously identified, and first approximations to the spin orientations at several points around the precession cycle are obtained.

As the spin axis precesses, the rocket elevation of a given star varies so that the amplitude of its signal is modulated according to the response function of the star sensor. This modulation may be a prolonged appearance or disappearance of a periodic signal as the star crosses one boundary or the other of the elevation range of the sensor. It may be a momentary disappearance as it crosses a masked interval in the middle of the sensitive elevation range. In any event, the sequence of times at which significant modulation events occur in the amplitudes of the star signals is determined by the response function of the sensor and by the parameters of the precession motion: i.e. the celestial orientation of the precession axis, defined by $\alpha_c(p)$ and $\delta_c(p)$, the precession angular velocity ω_p , and the opening angle α of the precession cone. Only a particular combination of the precession parameters will lead to a predicted sequence of times of modulation events that matches the one observed. In practice we search for this combination with the aid of a computer. By successive approximations we obtain a set of parameters which minimizes

the sum of the squared deviations between the predicted and observed times, and in this way we establish the celestial orientation of the precession frame and the precession cone angle. Any object whose precession azimuth and elevation is known can now be located in the celestial frame by a simple transformation.

The fourth step is the determination of the precession azimuths of the X-ray sources. Already, by comparing the bearing distribution plots for the X-ray detector and star sensor data described earlier, the relative average bearings (i. e. relative precession azimuths) of the X-ray sources and the various stars can be established. Now that the stars are identified, the absolute average bearings of the X-ray sources can be determined, and these are the precession azimuths.

The fifth step is the determination of the precession elevations of the sources. This can be accomplished, in principle, by measuring the variation of a source's bearing during the precession cycle, since, as previously noted, the amplitude of this variation depends on α and $\lambda_p^{(o)}$. This method amounts to a kind of "triangulation" of the source with a base line equal to twice the opening angle α of the precession cone. For the small values of α that occurred in the ASE-MIT experiments, the accuracy of this method is not very high.

A more accurate method for the determination of $\lambda_p^{(o)}$ is based on an analysis of the variation in the counting rate from a source which is caused by the periodic change in the elevation of the source in the rocket frame. By inspection of the bearing distribution we select an interval of bearing within which essentially all of the counts from the source occur. For each count recorded in this interval we compute the quantity $l = \lambda_r^{(d)} - \alpha \cos(\phi_p^{(s)} - \phi_p^{(o)})$ where $\phi_p^{(o)}$ is the precession azimuth of the source as previously determined, and $\lambda_r^{(d)}$ is the rocket elevation of the

detector axis. If α and $\lambda_p^{(d)}$ is sufficiently small, then to a good approximation $l = \lambda_p^{(d)}$ when $\phi_p^{(d)} = \phi_p^{(o)}$; i.e. at the moment when the source transits the meridian plane of the detector in the precession frame (see Eq. 5). Moreover, if $\lambda_p^{(o)}$ lies with range from $\lambda_r^{(d)} - \alpha$ to $\lambda_r^{(d)} + \alpha$, then at some time during the precession cycle the detector axis sweeps across the source. At this time $\lambda_r^{(o)} = \lambda_r^{(d)}$, $l = \lambda_p^{(o)}$ (see Eq. 5), and therefore the counting rate plotted against l shows a maximum for a value of l equal to the precession elevation of the source. An example of such a distribution is shown in Fig. 30. When λ_p does not lie in the range from $\lambda_r^{(d)} - \alpha$ to $\lambda_r^{(d)} + \alpha$, one can still calculate the expected variation of the counting rate as a function of l from the known response function of the detector, and for any assumed value of $\lambda_p^{(o)}$. One can then adjust $\lambda_p^{(o)}$ to obtain the best fit of the computed variation to the observed one, and in this manner one can obtain an estimate of the precession elevation of the source.

In the case of a detector with a modulation collimator whose response maxima are separated by an angle smaller than 2α , the plot of counting versus l will show several maxima at values of l given approximately by the equation

$$l_n = \lambda_p^{(o)} \pm \arctan(na).$$

where a is determined by the dimensions of the collimator. An example of such a distribution is shown in Fig. 31.

4.0 OBSERVATIONAL RESULTS

4.1 The Crab Nebula

The source whose coordinates and angular dimensions are best known is that coincident with the Crab Nebula. As already mentioned, the information concerning this source comes mainly from the observation of the occultation of the Crab Nebula by the Moon performed by the NRL group (which named the source Tau XR-1).⁽⁴⁾ The rocket was attitude -

controlled and carried two X-ray detectors which acquired the X-ray source 150 sec. after launch and observed it for 240 sec. thereafter, during which time the edge of the Moon swept across the Crab Nebula in the manner shown in Fig. 23. The counting rates of the two detectors, and their sum are plotted as functions of time in Fig. 24. Shown in the same figure is the time derivative of the total counting rate, which represents the distribution of the X-ray source in the direction perpendicular to the advancing edge of the Moon. From these results, it was possible to show that the angular diameter of the X-ray source was about 1 arc minute, and that its center was close to the center of the visible nebula.

4.2 The Sources Near the Galactic Center

Let us consider next the complex of sources within 25° of the galactic center which includes the source in Scorpio, named ScoX-1 by the ASE-MIT group, the first X-ray source to be discovered and the strongest detected thus far.

Figure 25 illustrates the determination of the position of ScoX-1 performed by the NRL group by means of a slowly-spinning rocket in April 1963.⁽³⁾ The detector had a field of view about 10° full width at half maximum. The lines with arrows are traces of the detector's axis on the sky map during different spins; the numbers along these lines are counting rates. The circles are lines of equal counting rates, whose common center represents the source position.

Figure 26 shows the results of another flight carried out by the NRL group, with similar instrumentation, in June 1964.⁽¹¹⁾ Shaded segments indicate portions of scan where the X-ray counting rate was clearly above background. Circles are positions assigned by the authors to the X-ray sources held responsible for these increases in counting rate. Of the sources near the galactic center, only ScoX-1 (indicated as 1) gave a clearly separate peak. The other five were unresolved and, therefore, the results concerning these sources were somewhat tentative.

In addition to the sources near the galactic center, the instruments aboard the NRL rocket detected also two clearly resolved sources in Cygnus

From Bowyer et al, Science 146 912 (1964)

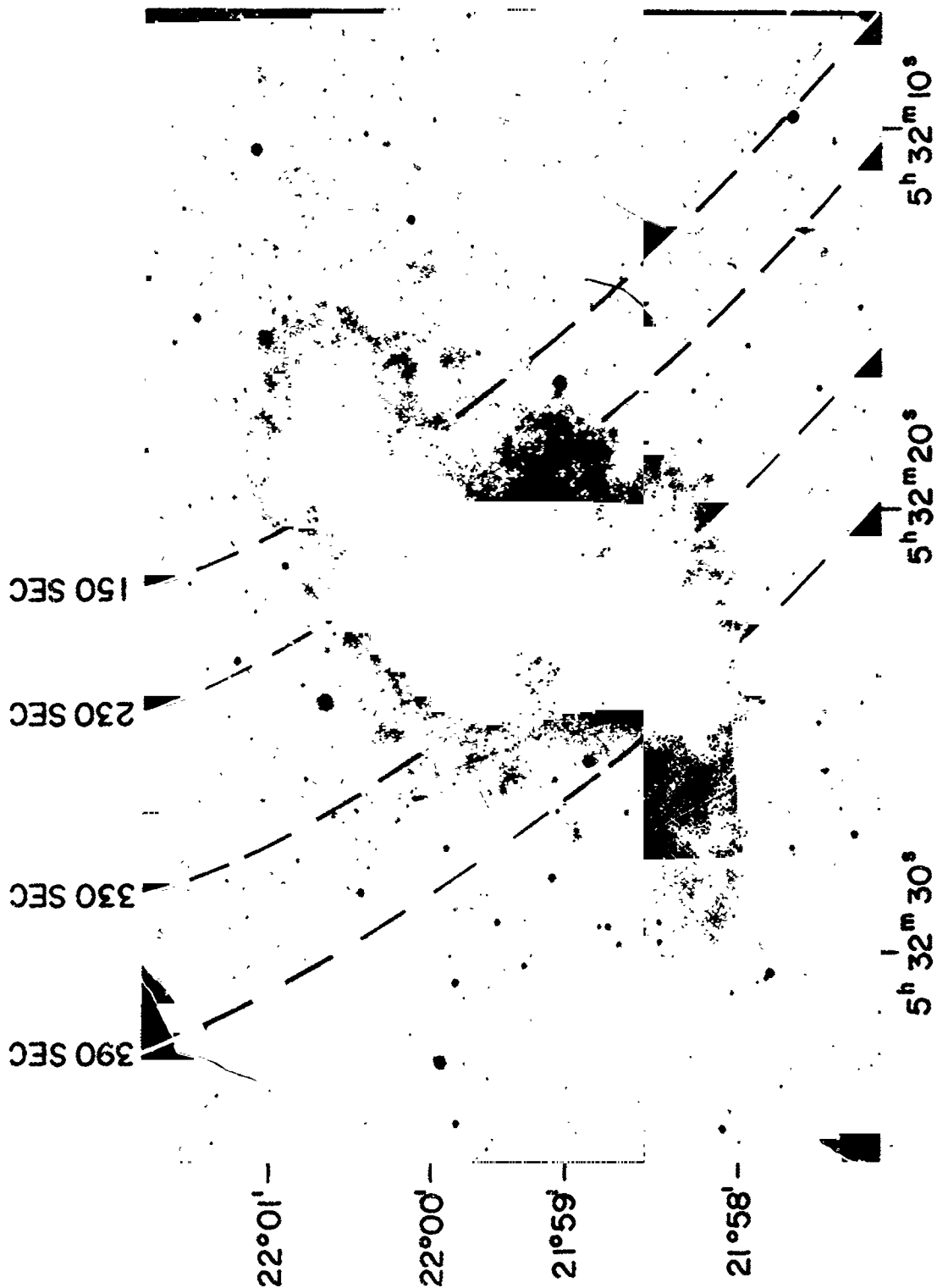


Fig. 23 Position of the edge of the Moon superimposed on a photograph of the Crab Nebula during NRL rocket flight. The maximum rate of change of the observed counting rate from the X-ray detector occurred at 230 sec; thus the centroid of the X-ray source distribution lies along the dashed line marked 230 sec.

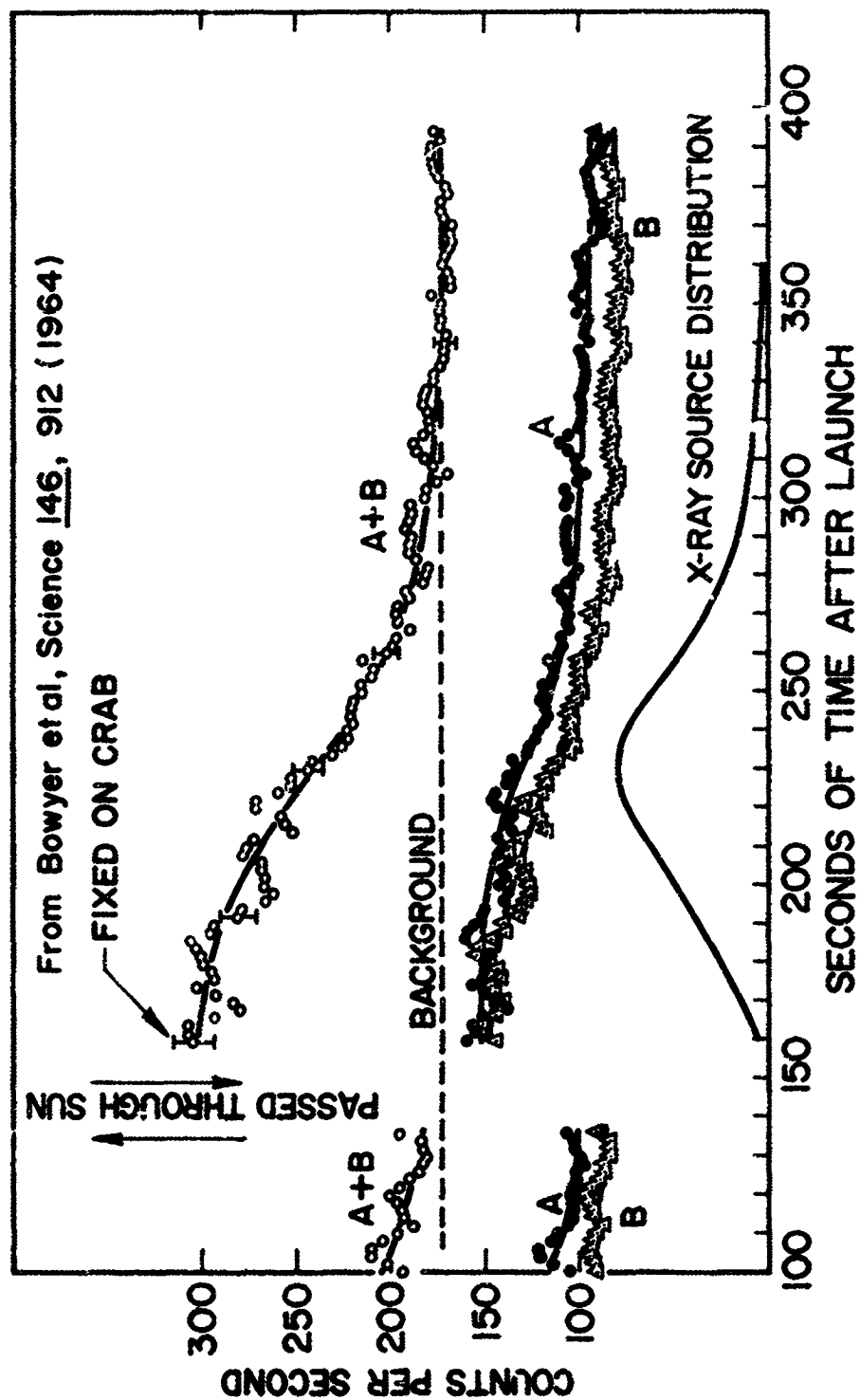


Fig. 24 Counting rates of the X-ray detectors A and B during the NRL rocket flight observing the occultation of the Crab Nebula by the Moon. The solid curve at the bottom is minus the time derivative of the A and B counting rate.

From Bowyer et al, Nature 201, 1307 (1964)

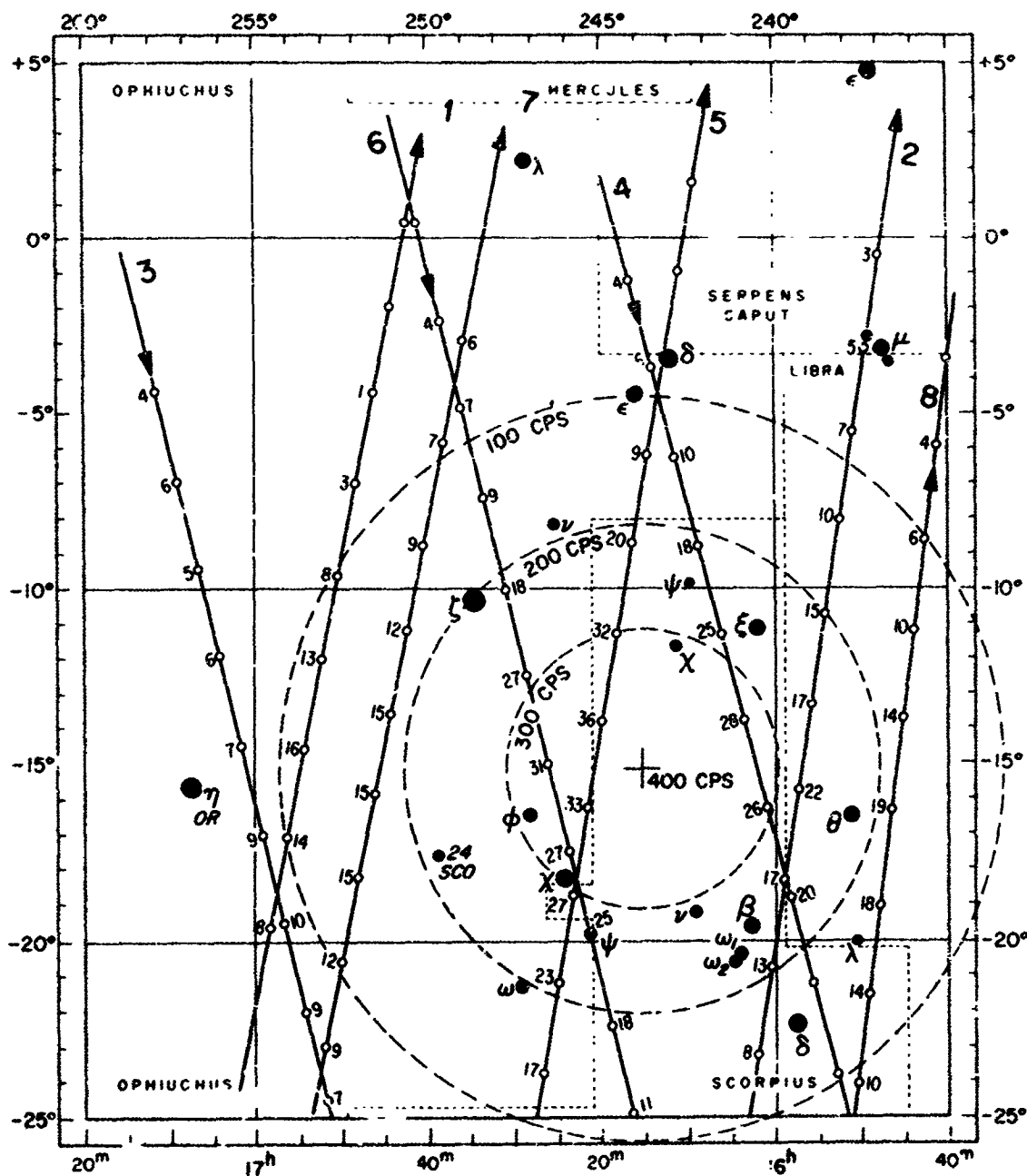


Fig. 25 Observation of the X-ray source in Scorpio by the NRL group. Solid curves show motion of the detector axis during successive passes over the region of the sky containing the source. Dashed circles are contour of equal counting rates consistent with observed counting rates. The centroid of these contours gives the best location of the source.

From Bowyer et al, Science 147 394 (1965)

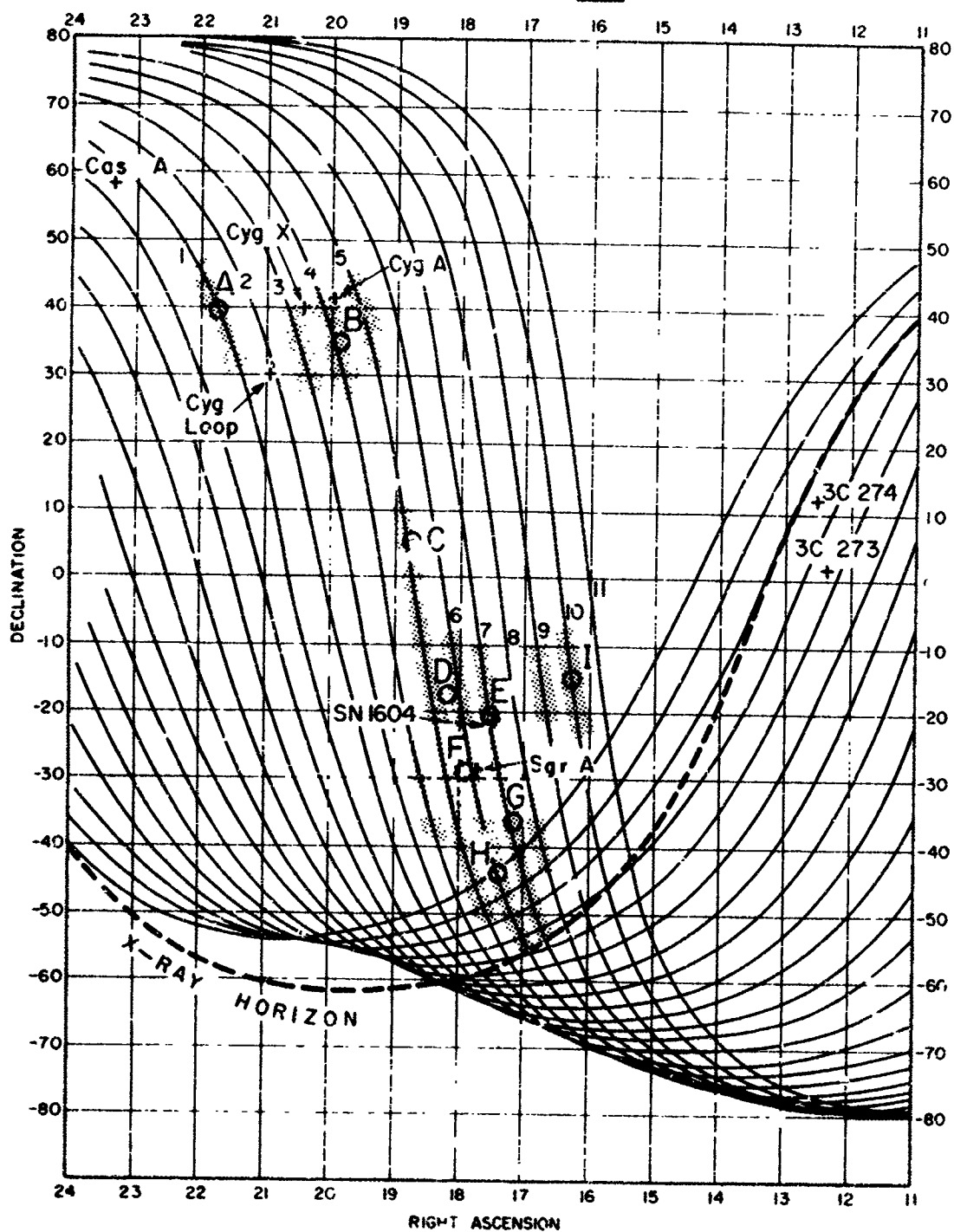


Fig. 26 Locations of X-ray sources observed during an NRL rocket flight. Solid curves represent the path of the detector axis during the flight. Shaded regions indicate times when excess counting rates were observed and circles indicate estimates of source locations.

(A and B in Fig. 26), and one unresolved source in Serpens. We shall return to these observations later.

Accurate data for some of the X-ray sources appearing in the region of the sky near the galactic center were obtained by the ASE-MIT group with a rapidly spinning rocket flown in October 1964.⁽¹²⁾ The rocket carried three banks of Geiger counters provided with collimators having fields of view in the shape of narrow slits (GV10, GH0, GH20) and one bank of Geiger counters provided with a modulation collimator. Figure 27 shows the fields of view of these detectors and of the star sensors in the frame of reference of the spinning rocket. Figure 28 shows the regions of the sky explored by the three detectors with narrow-slit collimators, and the positions of three sources, clearly identified by these observations. One is ScoX-1; the second lies also in the constellation Scorpius and is denoted as ScoX-2; the third lies in Sagittarius and is denoted as Sgr X-1.

Let us discuss in more detail the observational evidence obtained in these experiments. Consider first the results of counter GV10, whose direction of scan was perpendicular to the long side of the collimator's slit. Figure 29 shows the bearing angle distribution of the counts with respect to β -Ceti. The sharp maximum at A is due to ScoX-1; it affords an accurate determination of the azimuth of this source in the precession frame of reference placing it on the arc A in Fig. 28. Moreover, the variation of the counting rate due to ScoX-1 during the precession cycle shows that the detector's axis came closest to ScoX-1 when its elevation in the precession frame was a maximum. This observation places a lower bound to the elevation of ScoX-1, as indicated by the dotted line in Fig. 28. The smaller and broader maximum between B and C in Fig. 29 is due to a number of unresolved sources, including Sgr X-1, ScoX-2 and probably other sources near the galactic plane. These sources must lie in the cross-hatched region between the arcs of great circles marked B and C in Fig. 28.

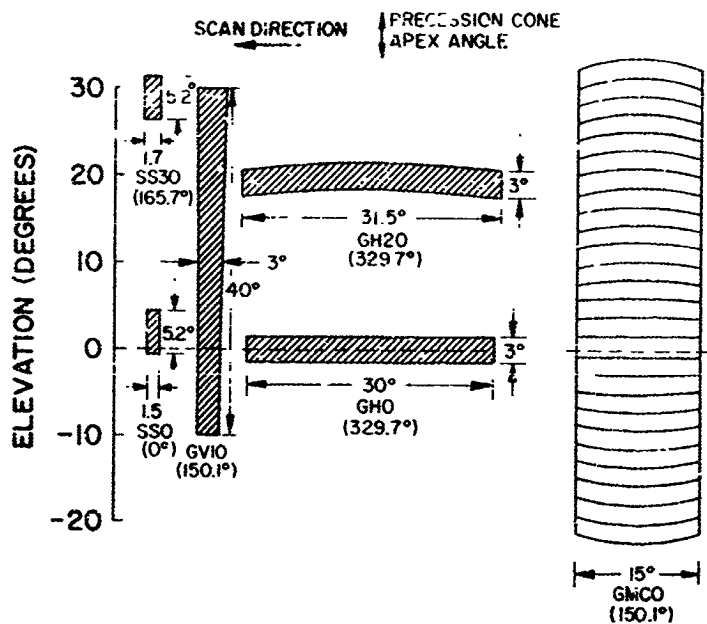


Fig. 27 Fields of view of the detectors used by the ASE-MIT group in the October 1964 rocket flight, shown on a rectangular grid plot of the rocket frame of reference. The number in parentheses below the instrument designation is the rocket azimuth of the detector axis.

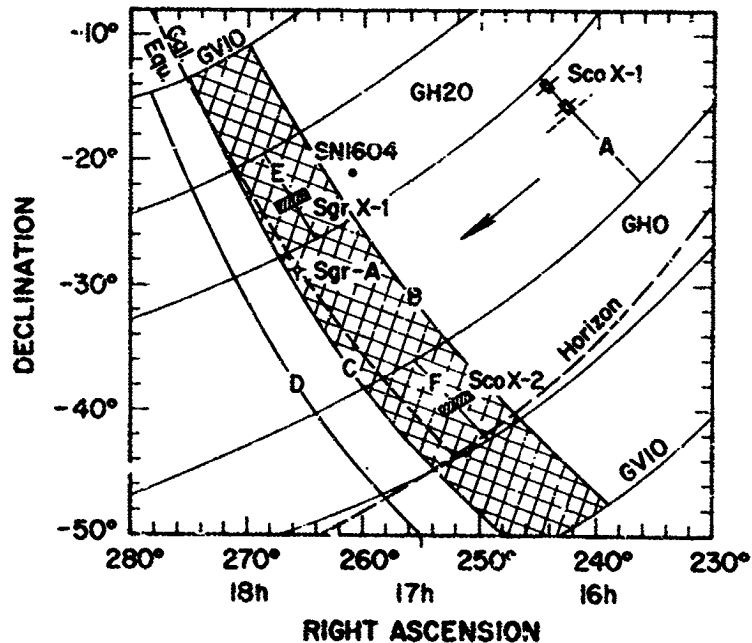


Fig. 28 X-ray source locations determined during ASE-MIT rocket flight of October 1964. The region bounded by the arcs marked by GV10 has been scanned. Sources are found to lie along the solid curves marked A, D, E, and F. The region between the curve marked B and C contains an unknown number of unresolved sources.

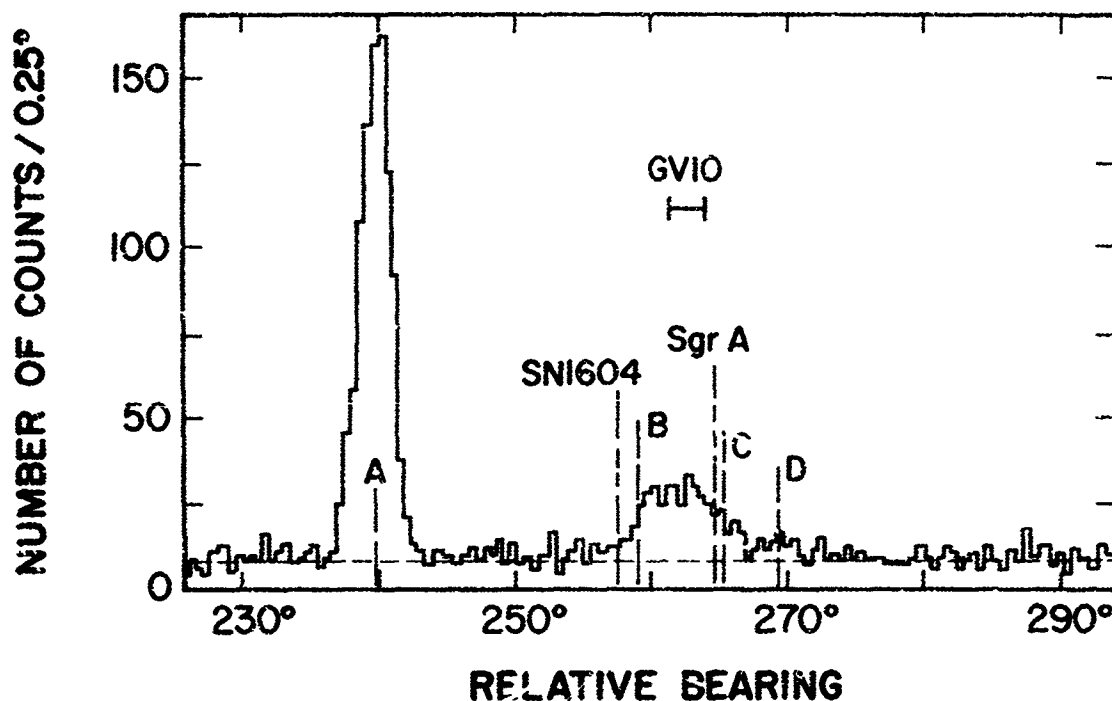


Fig. 29 Bearing angle distribution of counts observed with detector GV10 during October 1964 rocket flight. The abscissa represents the bearing angle of the detector axis with respect to complete the average bearing angle of β -Ceti. Full width of half maximum of detector response is indicated.

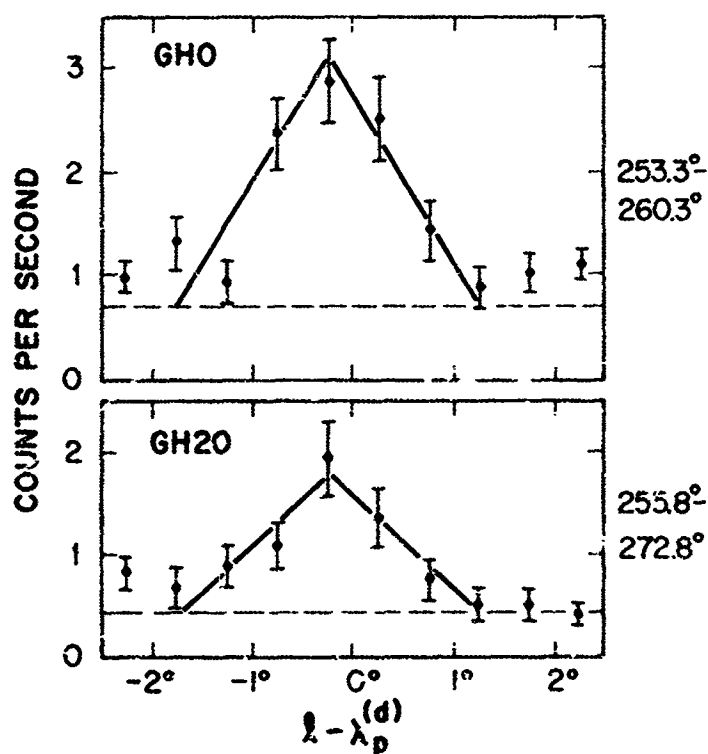


Fig. 30 The distribution in relative elevation of counting rates observed with detectors GH0 and GH20 during October 1964 rocket flight. Superimposed on the observational points are the theoretical angular responses of the detectors. The abscissa is the elevation of the detector axis in the precession frame at the moment of closest approach to the source minus the (fixed) elevation of the detector axis in the rocket frame. The bearing angle range with respect to β -Ceti is indicated at the right side of each curve.

Still another small maximum in the bearing distribution suggests the existence of a weak source along the arc marked D, although it is not clear that D is separate from the source region between B and C.

Consider next the results of counter banks GH0 and GH20. Neither of these counters saw ScoX-1. The fact that this source never entered the field of view of GH20 further restricts the possible range of elevation angles for ScoX-1, placing it below the region explored by the detector (see Fig. 28).

The curves giving the bearing angle distributions of counts recorded by both GH0 and GH20 had maxima, indicating the presence of sources lying within the bands scanned by the two detectors, and belonging to the source complex between the great circles B and C detected by GV10. The positions of the maxima determine the azimuthal angles of the sources in the precession frame, placing the sources along the arcs of great circle marked E and F in Fig. 28. Because the long dimensions of the slits representing the fields of view are in the direction of the scan, the maxima are rather flat and the azimuth determinations provided by counters GH0 and GH20 are not as precise as those provided by counter GV10. On the other hand, the narrow dimensions of the slits in the direction perpendicular to the scan affords an accurate determination of the elevation angles of the two sources in the precession frame. To obtain this information, appropriate "windows" were chosen around the azimuths of the sources, and the counts recorded within these windows, at various phases of the precession cycle, were plotted against the quantity $1 - \lambda_r^{(d)}$ (see Section 3.2) which is approximately the relative elevation of the detector's axis at the center of the window. The results for counters GH0 and GH20 are shown by the graphs in Fig. 30. In both graphs, the counting rate is a maximum near the middle of the precession cycle, i.e., when the elevation of the detector's axis in the precession frame is nearly equal to its elevation in the rocket's frame. Thus, Sgr X-1 lies

near the center of the band scanned by GH20 and ScoX-2 lies near the center of the band scanned by GH0.

Consider, finally, the results of counter bank GMC0 provided with a modulation collimator of about 30 arc minutes resolution. Figure 31 shows the variation of its counting rate due to ScoX-1 during the precession cycle. A previous experiment with a modulation collimator of higher resolution had shown that the angular dimension of ScoX-1 was less than 7 arc minutes.⁽¹³⁾ The completeness of the modulation observed with the present detector is entirely consistent with this result. Moreover, the position of the maxima makes it possible to place ScoX-1 on one of the circles of constant elevation corresponding to the transmission maxima of the modulation collimator at the time when a maximum of the counting rate is observed. Two of these circles fall between the limits of elevation previously determined, thus giving for ScoX-1 the two possible locations shown in Fig. 28.

Table I lists the most likely positions of ScoX-1, ScoX-2 and Sgr X-1, as obtained from the observations just described.

Data relative to the same region of the sky were also obtained by the Lockheed group, by means of an attitude controlled rocket flown in October 1964.⁽¹⁴⁾ The rocket carried three detectors with collimators having fields of view in the shape of narrow slits, whose long dimensions were arranged at different angles to the rocket's axis. Thus, from the relative delay between the transit times of a given source through these fields of view, it was possible to obtain information concerning the elevation of the source in the rocket's frame of reference. The rocket was programmed to execute four different scans during its flight. Figure 32 shows the arcs traced on the sky by the normals to the detectors during these scans; the rectangles at the beginning of scan 1 show the fields of view of the three detectors, denoted as T(top), C (center), B(bottom).

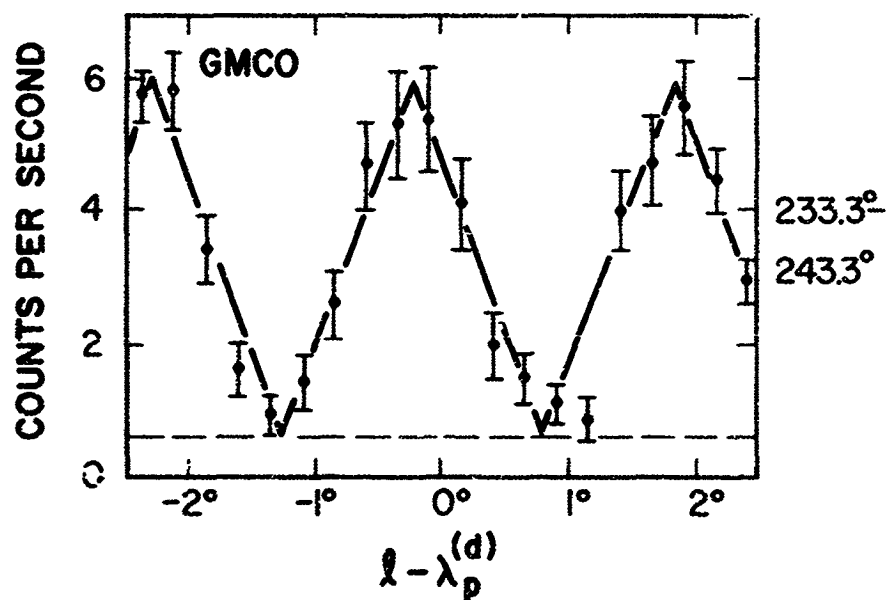


Fig. 31 Distribution in relative elevation of the counting rates from ScoX-1 observed with detector GMCO which was provided with a modulation collimator. Superimposed on the observational points is the theoretical angular response of the collimator.

SOURCE	RIGHT ASCENSION	DECLINATION
Sco X-1	$16^h 12^m \pm 2^m$	$-15.6^\circ \pm 0.5^\circ$
	$16^h 19^m \pm 2^m$	$-14.0^\circ \pm 0.5^\circ$
Sco X-2	$16^h 50^m \pm 7^m$	$-39.6^\circ \pm 0.9^\circ$
Sgr X-1	$17^h 44^m \pm 7^m$	$-23.2^\circ \pm 0.9^\circ$

Table I X-ray Source Locations Determined During October 1964 Rocket Flight .

From Fisher et al, Preprint (1965)

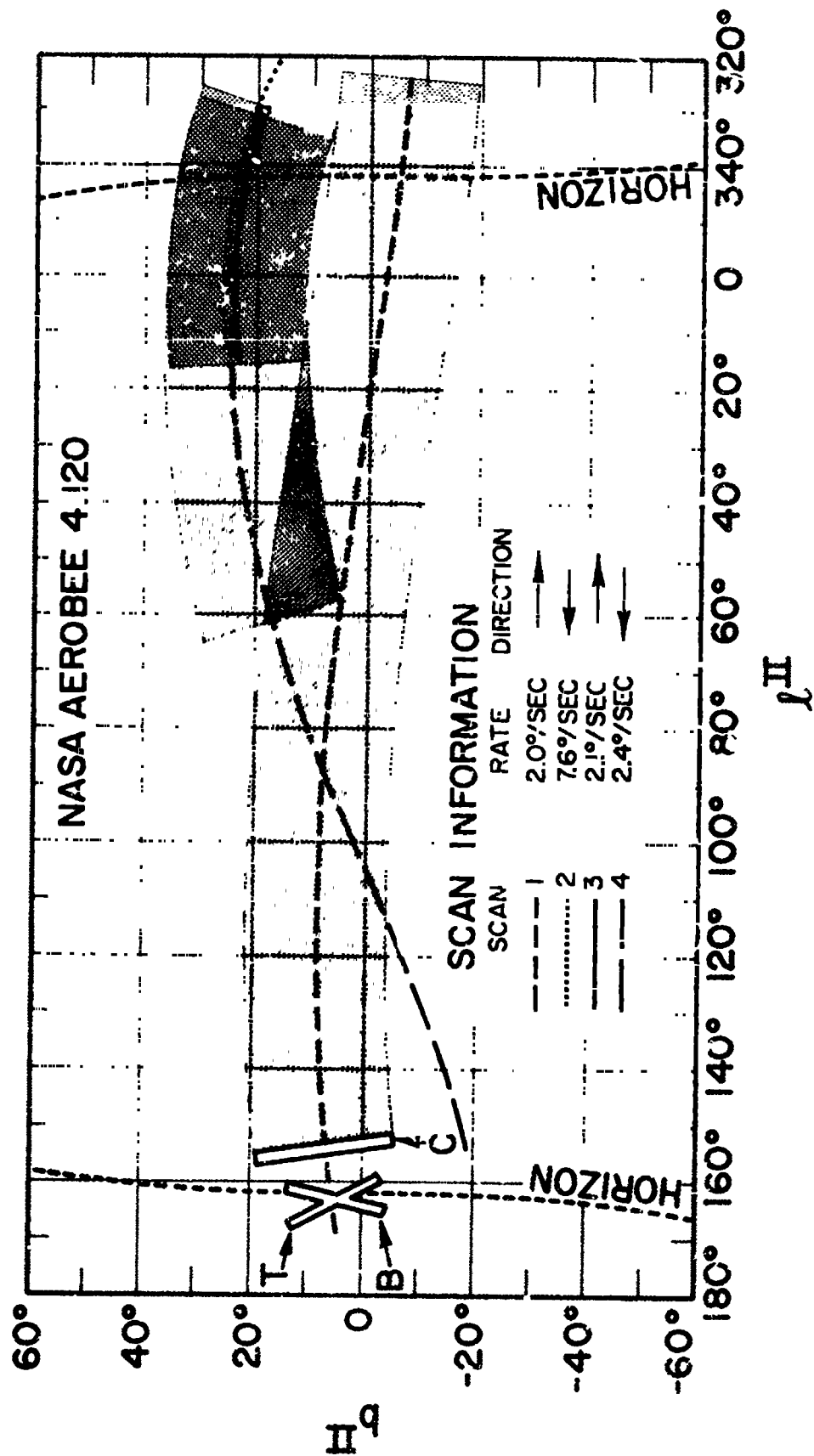


Fig. 32 Traces of detector axes during Lockheed rocket flight. Rocket was provided with attitude control.

The shaded areas indicate the bands scanned by detector C.

ScoX-1 was detected during scans #2, 3, 4. All three counters T, C, and B gave useful data during the two slower scans (#3 and 4). They provided the following determination for the position of this source:

$$\begin{array}{ll} \text{right ascension:} & 16^{\text{h}} 14^{\text{m}} \pm 1^{\text{m}} \\ \text{declination:} & -15^{\circ} 36' \pm 15' \end{array}$$

Only counter C provided useful data during scan #1, which ran along the galactic equator. The counting rate went through several maxima, indicating the existence of a number of sources. However, only the azimuthal angles of these sources in the rocket's frame of reference could be determined. The arcs of great circle corresponding to the sources near the galactic center are shown in Fig. 33 as narrow bands having a width equal to the experimental uncertainty in the angular measurement.

In Fig. 34 the results of the NRL group, the ASE-MIT group and the Lockheed group are summarized and compared. Concerning the sources near the Galactic center, we note the following:

- (a) Both alternate positions for ScoX-1 found by the ASE-MIT group fall within the circle of uncertainty of the determination made by the NRL group. One of them is consistent with the position given by the Lockheed group. As already noted, we know from the results of the ASE-MIT group that the angular size of ScoX-1 is less than 7 arc minutes.
- (b) The position for Sgr X-1, as determined by the ASE-MIT group, is about 1° from the arc of the great circle corresponding to one of the sources found by the Lockheed group. This discrepancy may be accounted

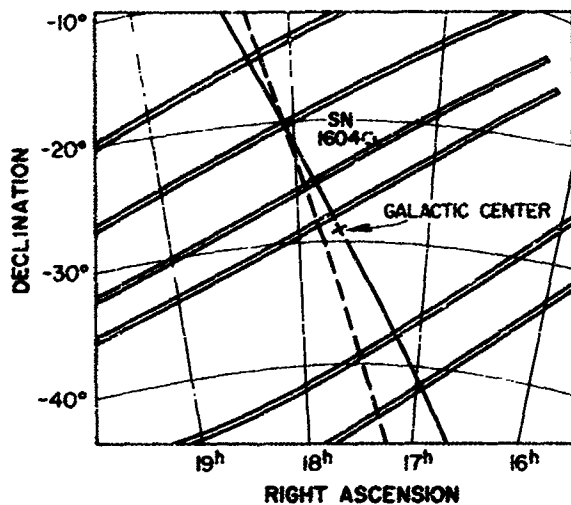


Fig. 33 X-ray source locations in the vicinity of the galactic center determined during Lockheed rocket flight. Dashed line is the path of the detector axis and the narrow bands normal to this line represent regions of the sky containing X-ray sources.

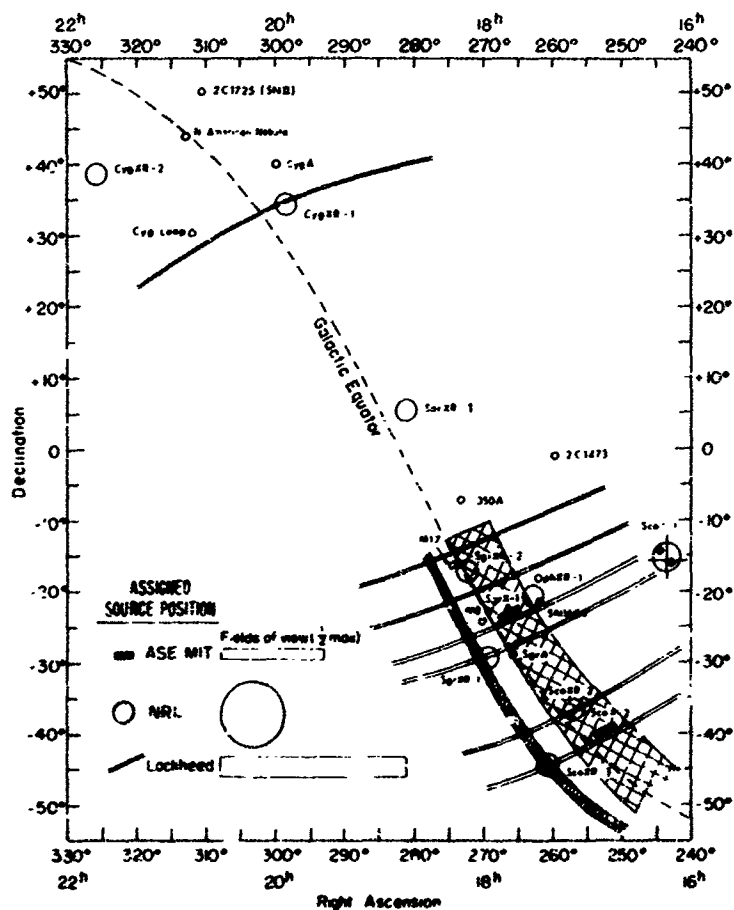


Fig. 34 X-ray source locations as determined during three 1964 rocket flights. ASE-MIT locations have been given in Figure 29; NRL locations have been given in Figure 23, and Lockheed locations have been given in Figure 34.

for by experimental errors; thus, the sources observed by the two groups may be the same. However, Sgr X-1 does not lie within the circle of uncertainty of any of the sources found by the NRL group. The closest NRL source is OphXR-1 whose center lies 5° from the ASE-MIT position of Sgr X-1. The existence of a source in this position is not consistent with the ASE-MIT data.

(c) Sgr X-1 is 5° from the Kepler supernova remnant SN 1604. Thus, the ASE-MIT observation rules out the existence of a detectable X-ray source in this position, and the tentative identification by the NRL group of their OphXR-1 source with SN 1604⁽¹¹⁾ does not seem to be correct.

(d) The position for ScoX-2, as determined by the ASE-MIT group, is about 1° from the arc of great circle corresponding to one of the sources seen by the Lockheed group. Again, the discrepancy may be due to experimental errors, and the sources seen by the two groups may be the same. On the other hand, ScoX-2 lies about 5° from the nearest source reported by the NRL group (ScoXR-2); the ASE-MIT results are not consistent with the existence of an X-ray source in this position.

(e) The NRL source SgrXR-2 lies half way between the arcs of great circle about 12° apart, on which the Lockheed group located two separate sources. Possibly the peak of counting rate in the NRL observations resulted from the combined effects of these two sources.

(f) In addition to these two sources and to the ASE-MIT sources SgrX-1 and ScoX-2, the Lockheed results indicate the existence of at least two other sources near the galactic center. One of them may coincide with NRL source Sgr XR-1. It appears difficult to identify the other with any

of the NRL sources, unless there is a sizeable error in the position of ScoXR-2 quoted by NRL.

(g) Sgr A, the radio center of the Galaxy, is at most a weak X-ray source compared with the other sources nearby.

4.3 Other Sources

Early observations by the ASE-MIT group suggested the presence of X-ray sources in the general region of Cygnus.^(1, 2) As noted previously, the NRL group detected two sources, Cyg XR-1 and Cyg XR-2 in this region (see Fig. 34). One of them (Cyg XR-2) lies near the arc of great circle where also the Lockheed group located an X-ray source. Cyg XR-2 was not scanned by the Lockheed group. Neither Cyg XR-1 nor Cyg XR-2 coincides with the Cygnus loop or with Cyg A.

Lastly, the NRL observations indicate the existence of a source in Serpens; a small maximum in the counting rate observed by the Lockheed group in scan #1 may be due to the same source.

4.4 Spectral Information and Flux Estimates

Some information on the spectra of the X-ray sources has been obtained from absorption measurements as well as from the pulse-height distributions observed with proportional counters and with scintillation counters. Partly because of the nature of the measurements, partly because of the limited statistical accuracy, none of the available results affords a direct determination of the spectral distribution, i.e., of the function $j(E) dE$ giving the energy flux of X-rays with photon energy between E and $E + dE$. Rather certain a priori assumptions had to be made on the form of the spectral function $j(E)$; the experimental results

could then be used to compute the free parameters entering in the expressions for $j(E)$, and, in some cases, to rule out certain types of spectral functions.

The spectral functions usually considered are:

Power Law:

$$j(E) dE = \text{const.} \frac{dE}{E^\alpha} \quad (9)$$

Synchrotron radiation and inverse Compton effect are likely to produce spectra of this kind.

Exponential Law:

$$j(E) dE = \text{const} \times \exp(-E/kT) dE \quad (10)$$

Spectra of this kind are characteristic of low-Z, fully ionized, optically thin, clouds containing electrons with a Maxwellian velocity distribution corresponding to a temperature T . In this case, the process responsible for the X-ray emission is bremsstrahlung. (In the presence of incompletely ionized matter with Z greater than about ten, there would be a substantial contribution from free-bound transitions, giving rise to characteristic discontinuities in the spectrum).

Planck's Law:

$$j(E) dE = \text{const} \frac{E^3 dE}{e^{E/kT} - 1} \quad (11)$$

This law, characterizes the radiation from a black body at a surface temperature T .

4.4.1 The Crab Nebula

The NRL group in their Nov. 1964 flight observed the Crab Nebula with two X-ray counters provided with mylar windows 1/4 mil

and 1/2 mil thick respectively. The measured counting rates (2.7 and 1.6 per cm² sec) were consistent with a power-law spectrum of the type

$$j(E) dE = \text{const} \frac{dE}{E^{1.1}}$$

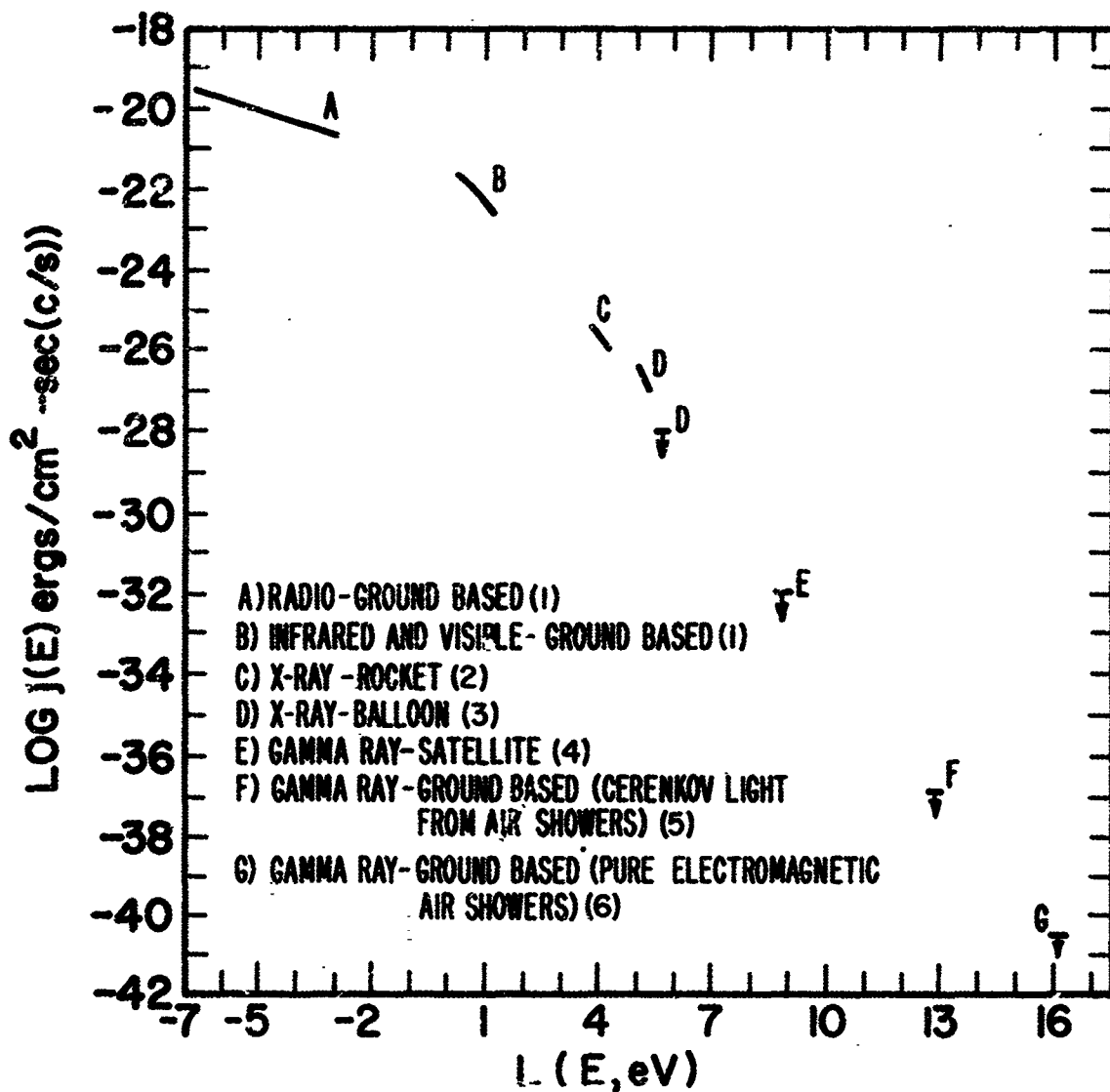
The energy range to which this result applies extends from 1.2 to 4.0 keV.

The Crab Nebula was also observed by G. Clark by means of a scintillation counter flown with a balloon in July 1964.⁽⁵⁾ The pulses were analyzed in four channels corresponding to (nominal) energies from 15 to 28, from 28 to 42, from 42 to 62 and greater than 62 keV. The counting rates in the three lower channels (after subtraction of background and correction for atmospheric absorption) were consistent with a power-law spectrum of the type:

$$j(E) dE = \frac{\text{const}}{E^2} dE$$

The higher channel did not contain any statistically significant signal, thus placing an upper limit to the flux. This upper limit indicated an increase in the logarithmic slope of the spectrum beyond 62 keV.

The experiments described above provided information not only on the shapes of the spectrum but also on the absolute values of the flux in the two regions explored. It is thus possible to combine their results into a single spectrum extending from about 1 to about 60 keV. It is also possible to compare the results relative to this range of energy with the flux measurements in the visible and in the radio regions of the electromagnetic spectrum, and with upper limits that have been obtained by various experimenters for the flux in the γ -ray region, from about 10^8 eV to about 10^{15} eV. The results of this comparison are summarized in Fig. 35. It



- (1) C. R. O'Dell, Ap. J. 136, 809 (1962)
- (2) H. Friedman (unpublished)
- (3) G. Clark, Phys. Rev. Letters 14, 91 (1965)
- (4) W. Kraushaar, G. Clark, G. Garmire, H. Helmken, P. Higbie and M. Agogino, Ap. J. 141, 845 (1965)
- (5) A. E. Chudakov, V. I. Zatespin, N. M. Nesterova and D. L. Daidiken, Proc. of Fifth Interamerican Seminar on Cosmic Rays, Vol V, pXLIV-1 (La Paz 1962)
- (6) K. Suga, I. Escobar, K. Murakami, V. Domingo, Y. Toyoda, G. Clark and M. LaPointe, Proceedings of the International Conference on Cosmic Rays, Jaipur (1963)

Fig. 35 Summary of experimental data on the spectrum of electromagnetic radiation from the Crab Nebula.

appears that the spectrum of the Crab Nebula may be approximated by a single power law with exponent of about 1 from a few eV to a few 10 keV. For higher energies, however, the spectrum becomes considerably steeper. Moreover, interstellar absorption must produce a "gap" in the spectrum which has not yet been observed, but whose detailed experimental investigation promises to afford important information on the composition of interstellar gases.

4.4.2 The Sources Near the Galactic Center

Early results of the ASE-MIT group on the atmospheric attenuation of X-rays from these sources (as observed with Geiger counters) were found to be consistent with a black-body radiation corresponding to a temperature of about 10^7 °K, without, however, providing any evidence for or against the assumption that the shape of the spectrum was of this particular form. Later results for ScoX-1 by the NRL group (based again on atmospheric absorption) gave an effective temperature between 2 and 3×10^6 under the assumption of a black-body spectrum. ⁽¹¹⁾

Additional data were obtained in 1964-1965 by the Lockheed group, the ASE-MIT groups and the NRL group. The results of the Lockheed group refer to ScoX-1 alone. They are based on observations made with the same three proportional counters that also provided the data on the location of this source ⁽¹⁴⁾ (T, C, and B in Fig. 32). Counters T and C had 5-mil thick Be windows, counter B had a 0.5 mil thick Al window. All counters were 4.0 cm deep and were filled to a pressure of 83 cm Hg with a mixture of 90 percent argon and 10 percent methane. From the computed efficiency curves, the estimated energy resolution of the counters and the associated circuitry, and the observed pulse height distributions, they obtained the

energy spectrum shown in Fig. 36. No significant signal was observed in the lowest channel so that only an upper limit could be placed to the flux in the 2-4 keV interval. This upper limit appears to indicate a sharp drop-off of the spectrum below 4 keV; however, it has been reported privately that the interpretation of the measurements in the 2-4 keV channel is affected by considerable uncertainty.

The ASE group obtained spectral data in a rocket flight carried out in August 1964, as well as in the rocket flight of October 1964, mentioned previously.⁽¹⁵⁾ The instrumentation of the August flight included a bank of Geiger counters with Be windows of 9.0 mg/cm^2 thickness, filled with argon to a gas thickness of 5.4 mg/cm^2 . The computed efficiency curve of this counter was checked by means of the beam from a tungsten target, windowless X-ray tube operated at different voltages from 1.8 to 10 keV. The counter bank was provided with a collimator which made it possible to separate the signals received from ScoX-1 and from the sources near the galactic equator.

At launch two filters, one of 7.0 mg/cm^2 Be (F-1) and one of 1.72 mg/cm^2 Mylar (F-2) were placed in front of the counters. During the flight, first one then the other filter was removed so that the counting rates with F-1 and F-2, with F-1 alone and with no filter could be measured. Data relative to essentially a full precession cycle are available for each of the three situations; therefore, no correction is needed for a change in the average angle of incidence of the radiation during the three measurements.

The results are summarized in Table II. Note, in the first place, that the spectral information obtainable from these data refers to the energy region for about 1 to about 10 keV. Note also that there is no

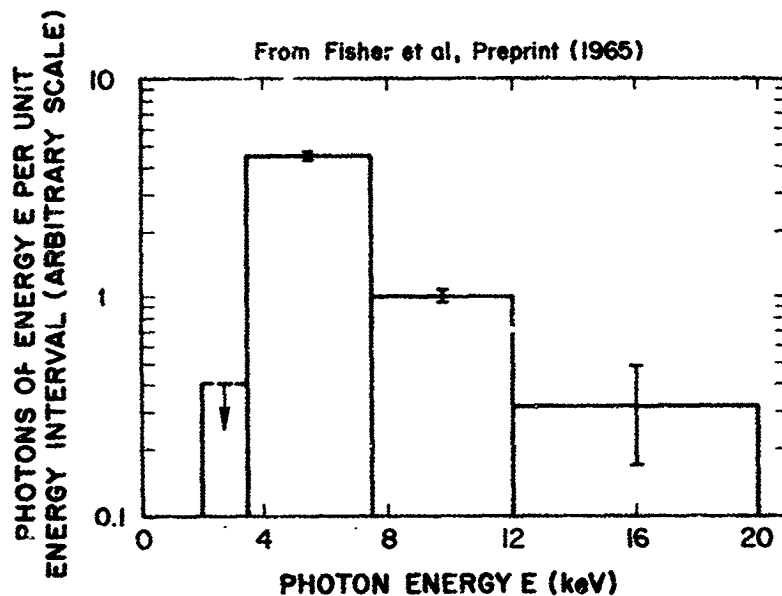


Fig. 36 Spectral distribution of X-rays from ScoX-1 as obtained from pulse height distribution of a proportional counter.

FILTER CONDITION	SOURCE REGION	COUNTING RATE MEASURED cts/sec	ATTENUATION RELATIVE TO NO FILTER
NO FILTER	SCOX-1	620 ± 20	1
F1	SCOX-1	440 ± 18	$0.71 \pm .04$
F1 + F2	SCOX-1	350 ± 17	$0.56 \pm .03$
NO FILTER	GAL CEN	350 ± 18	1
F1	GAL CEN	240 ± 18	$0.70 \pm .06$
F1 + F2	GAL CEN	210 ± 15	$0.62 \pm .03$
TYPICAL BACKGROUND RATE		30 cts/sec	

Table II Filter Absorption Data on X-ray Sources .

statistically significant difference between the attenuations observed from ScoX-1 and for the sources near the galactic plane. It turns out that the experimental results do not permit a distinction between the three types of spectra represented by Eqs. 6, 7, and 8. For each assumed type of spectrum, however, they provide a determination of the characteristic parameter, to wit:

$$\text{Power Law: } \alpha = 1.1 \pm 0.3$$

$$\text{Exponential Law: } T = (3.8 \pm 1.8) \times 10^7 \text{ } ^\circ\text{K}$$

$$\text{Planck's Law: } T = (9.1 \pm 0.9) \times 10^6 \text{ } ^\circ\text{K}$$

The data are not consistent with the sharp dropoff of the spectrum below 4 keV tentatively indicated by the Lockheed results.

The instrumentation of the October flight included a NaI scintillation counter, provided with a suitable collimator. The pulse-height distributions observed in the two source regions, with background subtracted, are shown in Fig. 37. The cut-off below 10 keV results from the electronic threshold. Above 10 keV, the three pulse-height distributions are significantly different. The distribution observed from ScoX-1 falls below the minimum detectable level at about 18 keV (a result consistent with a cut-off of the spectrum at about 15 keV). On the other hand, the combined spectrum of the sources near the galactic plane extends to higher energies.

If we now compare the Geiger counter data obtained in the August flight with the scintillation counter data obtained in the October flight, we reach the following conclusions.

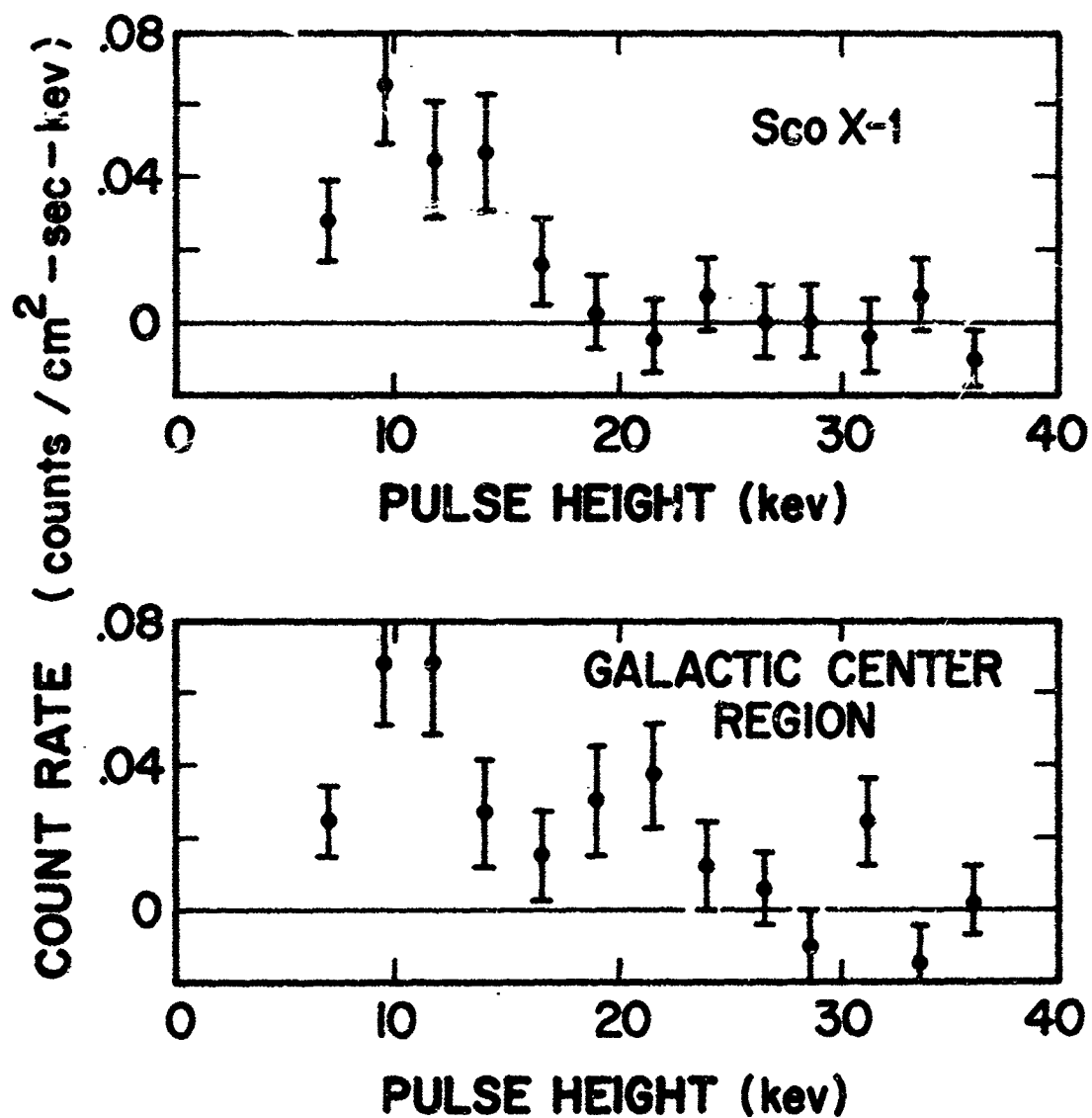


Fig. 37 Pulse height distributions of a Sodium iodide (NaI) scintillation detector, due to X-rays from ScoX-1 and from the galactic center region.

A black-body spectrum cannot fit both sets of data for either ScoX-1 or the sources near the galactic equator since such a spectrum falls off with increasing energy much more rapidly than the experimental results indicate. On the other hand, both a power law and an exponential law, with the appropriate values of the parameters mentioned previously, can account for the data obtained with the scintillation counter as well as with the Geiger counters. There is, however, evidence that the combined spectrum of the sources near the galactic equator is somewhat harder than that of ScoX-1.

The NRL group obtained spectral information on celestial X-ray sources both during the June 1964 flight, mentioned previously, and during a flight carried out in April 1965, whose results, so far, have been described only in a preliminary report.

In the June 1964 flight, ScoX-1 was observed at different altitudes during the descent of the rocket. From the measured atmospheric attenuation, it was concluded that of the flux detected at the highest altitude about 1/3 was accounted for by photons with energies above 2 keV and 2/3 by photons with energies between 1.2 and 2 keV.

In the April 1965 flight, the NRL group used four counters with the following characteristics: (1) argon filling, 1 mil mylar window; (2) argon filling, 1/4 mil mylar window; (3) neon filling, 1/4 mil mylar window; (4) helium filling, 1/4 mil mylar window. The relative counting rates of these detectors, which had very different spectral response curves, were found to be significantly different for different X-ray sources. These differences indicate differences in the spectra, ScoX-1 being one of the

sources which appeared to have the softest spectrum. The results concerning ScoX-1 could not be accounted for by a black-body spectrum. They also provided evidence for a strong increment of flux at long wavelengths, in marked disagreement with the tentative results of the Lockheed group.

To conclude this section, we summarize in Table III some estimates for the X-ray fluxes in two different spectral regions from the Crab Nebula, from ScoX-1 and from the source complex along the galactic equator, within 20° of the galactic center. Note that these estimates depend, among other things, on the assumed shapes of the spectra which are still quite uncertain.

4.4.5 Background Radiation

Since the earliest observations by the ASE-MIT group, the existence of an isotropic X-ray background has been indicated. Information on the background flux is summarized in Fig. 38. The ratios η , of the counting rate of the isotropic component to the peak \mathcal{N} counting rate from ScoX-1 for various experiments are plotted versus the solid angle or corresponding to the field of view of the respective measurements. This ratio is insensitive to the experimental conditions provided the spectra of ScoX-1 and the background are essentially similar. The ratio is: $\phi_B \cdot \mathcal{N} / \phi_{\text{Sco}}$ where ϕ_B is the background flux per unit solid angle and ϕ_{Sco} is the flux density from ScoX-1. Results of the ASE-MIT measurements show that η is roughly proportional to \mathcal{N} as is expected if the background consists of X-rays distributed isotropically, except for one result which is suspected to be in error because of a partial failure of the anticoincidence counter which rejected cosmic ray particles. All other

TABLE III
INTEGRATED ENERGY FLUX FOR VARIOUS X-RAY SOURCES AND TWO DIFFERENT
RANGES OF PHOTON ENERGY

Source	Spectral Range (keV)	Energy Flux (ergs)/cm ² sec	Remarks
Crab	1 to 10	2×10^{-8}	NRL Data
	20 to 30	$(6 \pm 2) \times 10^{-9}$	G. Clark Balloon Data
ScoX-1	1 to 10	$(1.6 \pm 0.4) \times 10^{-7}$	ASE Geiger Counter ** Data
	20 to 30	$< 6 \times 10^{-9*}$	ASE Scintillation Counter Data
Galactic equator (including Sgr X-1, ScoX-1 and probably several additional sources.)	1 to 10	$(0.4 \pm .1) \times 10^{-7}$	ASE Geiger Counter ** Data
	20 to 30	$(16 \pm 5) \times 10^{-9}$	ASE Scintillation Counter Data

* Represents 2σ deviation above background; no significant excess was observed.

* Assuming E^{-1} power spectrum.

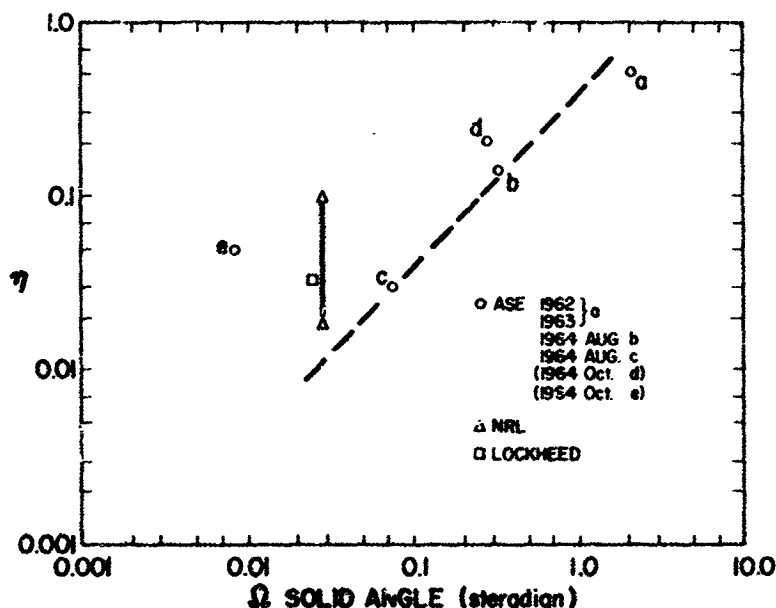


Fig. 38 Comparison of observations of the X-ray background made by various experimenters. The quantity η is the ratio of the counting rate of the background to peak counting rate of ScoX-I as observed in a given experiment.

data were obtained without an anticoincidence counter and, hence, it is understandable that they show slightly higher background fluxes. The estimate of the flux by NRL is based on the difference of the counting rate when the detector was looking upwards and downwards. The lower limit of NRL values of η is consistent with ASE-MIT results. Thus, the background component, which is proportional to the field of view of the detector, is estimated as about 6 count/(cm² sec ster) in the 2 ~ 8A band. If we consider the spectral response of the detector and the energy spectrum, the flux may be as much as 10 quanta/(cm² sec ster).

There is no evidence for anisotropy for any specific direction of galactic coordinate: e.g. say the direction of the Milky Way. Also, there is no positive indication to show a bright atmospheric horizon or any preferential local azimuth. All information indicates that a background flux of extraterrestrial X-rays truly exists; however, it cannot yet be excluded that a portion of this background originates from the Earth's magnetosphere.

ACR-111 111

This work was supported in part by the National Aeronautics and Space Administration under Grant NSG-106 and Contract NAS w-898, and by the United States Atomic Energy Commission under Contract AT(30-1) 2098.

REFERENCES

1. Giacconi, R., Gursky, H., Paolini, F. and Rossi, B. : 1962
Phys. Rev. Letters 9, 439.
2. Gursky, H., Giacconi, R., Paolini, F. and Rossi, B. : 1963
Phys. Rev. Letters 11, 530.
3. Bowyer, S., Byram, E. T., Chubb, T.A. and Friedman, H. : 1964
Nature 201, 1307.
4. Bowyer, S., Byram, E.T., Chubb, T.A., and Friedman, H. : 1964
Science 146, 912.
5. Clark, G.W. 1965 Phys. Rev. Letters, 14, 91.
6. Lukirskij, A. P., Rumsh, M. A., and Smirnov, L. A. : 1960 Opt. i
Spekroskopiya 9 , 265, 353
7. Oda, M. : 1965 Applied Optics 4, 143
8. Giacconi, R. and Rossi, B. : 1960 J.G.R. 65, 773.
9. Giacconi, R., Harmon, N., Lacey, R. F. and Szilagyi, Z.: 1965
J. Opt. Soc. Am. 55, 345
10. Giacconi, R., Reidy, W. P., Zehnpfennig, T., Lindsay, J.C. and
Muney, W.A. : 1965 Astrophys. J. 142, 1274
11. Bowyer, S., Byram, E.T., Chubb, T.A. and Friedman, H. : 1965 Science
147, 394.
12. Clark, G. W., Garmire, G., Oda, M., Wada, M., Giacconi, R.,
Gursky, H. and Waters, J. : 1965 Nature 207, 584.
13. Oda, M., Clark, G.W., Garmire, G., Wada, M., Giacconi, R.,
Gursky, H. and Waters, J. : 1965 Nature 205, 554.

17 JAN 66 24218

14. Fisher, P.C., Johnson, H.M., Jordan, W.C., Meyerott, A.J.,
and Acton, L.W. : submitted for publication to Astrophys. J.
(1965)
15. Giacconi, R., Gursky, H. and Waters, J.R. : 1965 Nature 207, 572